Competition and Coexistence of Screening Mechanisms in Ferroelectric Thin Films and Superlattices

UNIVERSITY OF CAMBRIDGE

Daniel Bennett

Supervisor: Prof. Emilio Artacho

Cavendish Laboratory
Department of Physics

This dissertation is submitted for the degree of
Master of Philosophy

St. John's College

October 2018

Declaration

I hereby declare that, except where specific reference is made to the work of others, the contents of this dissertation are original and have not been submitted in whole or in part for consideration for any other degree or qualification at this or any other university. This dissertation is substantially my own work and conforms to the University of Cambridge's guidelines on plagiarism, and contains nothing which is the outcome of work done in collaboration with others, except as specified in the text and references.

_____ _____

Daniel Bennett *Date*

Acknowledgements

I would like to thank my supervisor, Emilio Artacho, for helpful advice and discussions throughout the project. I am also very grateful for the funding provided by the EPSRC CDT in Computational Methods for Materials Science, without which this research would not have been possible.

The first-principles calculations in this project were performed on the Cambridge Service for Data Driven Discovery (CSD3) cluster.

Abstract

We present a theoretical and computational study of mechanisms that screen the depolarising field in ferroelectric materials, namely domains and two-dimensional electron gases. A more realistic electrostatic description of thin films, which accounts for the presence of a substrate has been derived. The electrostatic description of superlattices of alternating ferroelectric and paraelectric layers was also obtained. In both cases a modified Kittel law was observed for the domains which accounts for the substrates and the superlattice geometries. We review the model of coexistence between screening mechanisms for a ferroelectric thin film in a vacuum. Using the modified electrostatics, this model was extended to describe thin films on substrates and superlattices. It was found that the permittivities of the substrates and paraelectric layers extended the range of thicknesses where coexistence between the screening mechanisms can be sustained. First-principles calculations of monodomain thin films and superlattices were performed using the virtual crystal approximation to introduce a two-dimensional electron gas through interfacial defects. We observed the screening of the depolarising field by the two-dimensional electron gas, sustaining the polarisation within the materials.

Table of contents

Chapter 1

Introduction and Motivation

1.1 Ferroelectrics

Ferroelectric materials have a wide range of applications and are essential components of many modern devices [1]. A ferroelectric material is one with a spontaneous polarisation in the absence of an electric field. The direction of the polarisation can be reversed by applying an external electric field in the opposite direction. This phenomenon, known as polarisation switching, implies that a ferroelectric material's polarisation depends on its past and will thus exhibit hysteresis (see Figure 1.4). Using hysteresis as a memory function, ferroelectric capacitors have applications in non-volatile memory: ferroelectric RAM [2]. Due to the high geometric symmetry of many common ferroelectrics, there is a direct coupling between their mechanical and electrical properties. Hence, they must also be piezoelectric and pyroelectric. Thus, ferroelectric materials have potential for use in sensor applications [3]. Thin film ferroelectrics are typically preferred over their bulk counterparts because of their lower operating voltages and better compatibility with semiconductor devices [4]. One popular way of fabricating ferroelectric (and other ferroic) materials is in the form of a superlattice comprised of alternating layers of ferroelectric and paraelectric thin films [5–7]. The properties of these superlattices can vary considerably from those of the individual components, and can be tuned through the thickness and number of layers of each material.

It was originally thought that thin films could not be useful in practice due to problems such as the observed poor retention of ferroelectric polarisation, and polarisation fatigue: the decrease in spontaneous polarisation due to repeated polarisation switching [8]. Also, the polarisation induces bound charges at the interfaces of thin films, which, if left uncompensated for, will create an electric 'depolarising' field in the direction opposite to the polarisation. The energy cost of this depolarising field can reduce the polarisation or completely suppress

the ferroelectricity [9].

In practice, these effects are usually mitigated by a number of possible screening mechanisms. Using a capacitor geometry, where a thin film is sandwiched between two metal electrodes, the free charges in the electrodes can screen the bound charges, preserving ferroelectricity. Several interesting phenomena arise in thin films themselves that act as screening mechanisms. A microstructure of ferroelectric domains, regions polarised in different directions, can form in the material. The boundary between two domains is known as a domain wall. They are named in analogy to the magnetic domains that form in a ferromagnet. We will see in detail in the next chapter how these domains screen the depolarising field. One recent discovery is the formation of a two-dimensional electron gas (2DEG) at the interfaces of thin films and superlattices [10, 11]. These phenomena have generated great interest; there is evidence that 2DEGs can also enhance properties such as superconductivity capacitance in certain materials. Along with these potential applications, a better understanding of screening mechanisms could help to overcome problems such as depolarisation and fatigue. It is important to note here that the 2DEGs have that been experimentally observed were at polar interfaces, ones with polarisations that cannot be switched, but have only been indirectly observed at ferroelectric interfaces.

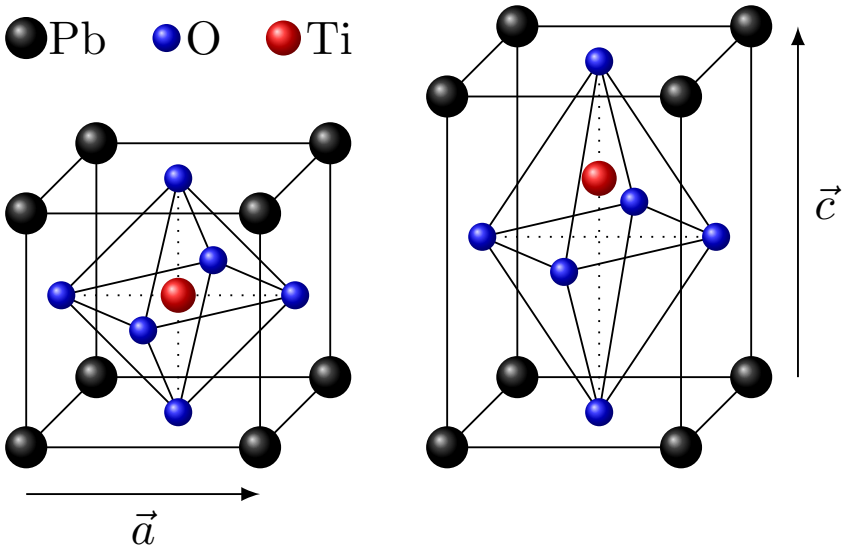

Fig. 1.1 Perovskite structure of PTO. Shown on the left is the cubic perovskite structure. Shown on the right is the tetragonal phase observed below the Curie temperature, T_C.

Several perovskites are examples of common ferroelectric materials. While perovskites have recently seen a massive increase in popularity in solar cell technology [12], they have always been the primary choice for ferroelectric devices. A perovskite is a material with the same crystal structure as calcium titanate ($CaTiO_3$). The chemical formula is ABX_3, where the A cations (e.g. Pb, Ba, Sr) are located at the corners of the unit cell, the B cations (e.g. Ti, Zr) are located at the cubic center and the X anions (typically O) are located at the cubic face centers (see Figure 1.1). Common examples of perovskites are lead titanate ($PbTiO_3$, PTO), barium titanate ($BaTiO_3$, BTO), strontium titanate ($SrTiO_3$, STO) and lanthanum aluminate ($LaAlO_3$, LAO), although STO and LAO are not nominally ferroelectric.

Pervoskites in the cubic phase are paraelectric: they do not have a spontaneous polarisation. This is due to the high symmetry of the cubic unit cell, and is typically observed at high temperatures. Below a certain Curie temperature, T_C, many perovskites undergo one or more structural phase transitions and become ferroelectric. Consider PTO, for example. At $T_C = 766$ K, it undergoes a structural phase transition from cubic to tetragonal, as illustrated in Figure 1.1. The atoms are displaced with respect to their original positions and as a result, the centres of positive and negative charge no longer coincide. This results in a net dipole moment and hence a spontaneous polarisation. The strain in the tetragonal unit cell and the distortion of the atomic positions are directly related to the polarisation. PTO in particular has a large c/a strain, approximately 6%, in comparison to other ferroelectric materials; the c/a strain in BTO is approximately 1%. In perovskites such as BTO, the spontaneous polarisation is primarily related to the cation-anion splitting, or distortion, of the TiO_2 layers. In PTO, the distortion of the PbO layers also plays a role, likely due to the rich chemistry of Pb.

1.1.1 Depolarising Field

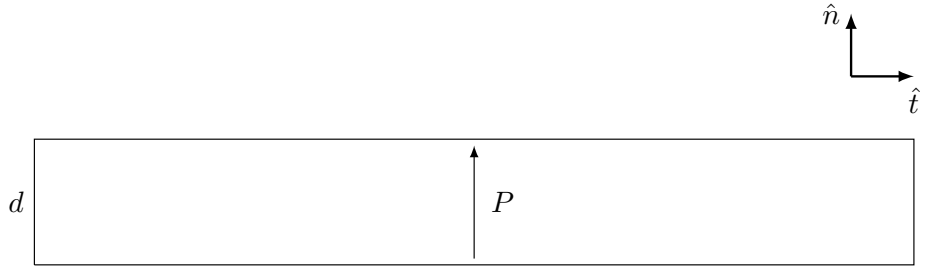

Fig. 1.2 A ferroelectric thin film with uniform polarisation P. The film extends infinitely in the directions tangential to the surface and has thickness d.

The appearance of the depolarising field, which is the origin of the screening mechanisms studied in this work, can be observed through a simple consideration of the boundary conditions in Maxwell's equations. Consider a uniform ferroelectric thin film with polarisation P in a vacuum, which is infinitely wide and has thickness d, as shown in Figure 1.2. The displacement field inside the film is normal to the surface and is given by

$$\vec{D} = \varepsilon_0 \kappa \vec{E} + \vec{P} \,, \tag{1.1}$$

where κ is the permittivity and $\vec{E}$ is the electric field inside the film. Because ferroelectric thin films are anisotropic, κ will be a diagonal matrix, the components of which are the permittivities in the normal and tangential directions. Since we are assuming the film to be infinitely wide, the displacement fields in the vacuum region must be zero. A nonzero displacement field outside the film would result in an infinite electrostatic energy as the field is integrated over the entire vacuum. Matching the displacement fields at the interface between the thin film and the vacuum region yields

$$\vec{D} = 0 \,, \tag{1.2}$$

which gives

$$\vec{E} = -\frac{1}{\kappa_c \varepsilon_0} \vec{P} \,, \tag{1.3}$$

where κ_c is the permittivity in the normal direction. This is known as the depolarising field. Note that it always opposes the polarisation. The energy *per unit volume* associated with the depolarising field is

$$U_{\text{dep}} = \frac{1}{2\kappa\varepsilon_0} P^2 \,, \tag{1.4}$$

which is positive and quadratic in the polarisation. This ideal example is the worst case scenario, but in more realistic situations the polarisation is reduced but not fully suppressed because of finite size effects, etc. The purpose of the screening mechanisms mentioned earlier is to reduce this depolarising field and sustain ferroelectricity.

1.2 Outline

Theoretical descriptions of ferroelectric materials have typically been for ideal ferroelectrics in a vacuum. The main motivation for this work is to study the screening mechanisms in more realistic situations. In order to do so, the electrostatic description of thin films on

substrates and in superlattices must be considered. This will allow us to determine the effects of substrates and the geometry of superlattices on the depolarising field. The main theoretical study of the electrostatics of ferroelectric thin films followed in this work is [13]. However, this analysis does not generalise well. Obtaining the correct electrostatic descriptions will not only allow us to describe the screening mechanisms in isolation, but will also lead to a more realistic model of coexistence between them.

An outline of this work is as follows: first, we review the electrostatic description of a ferroelectric thin film in a vacuum, and then consider the electrostatics of thin films on substrates and superlattices. We review the Landau theory of coexistence for ferroelectric thin films and then use the new electrostatic descriptions to extend this theory to thin films on substrates and superlattices. We also consider a more realistic version of the Kittel law for polydomain ferroelectrics. The theory presented in this work is not specific to any particular material. However, for illustrative purposes, we use thin films of PTO and PTO/STO superlattices as test cases.

Finally, we study the screening mechanisms using first-principles simulations, a cheaper and quicker way than fabricating and characterising the materials experimentally. Both domains and surface charges, which typically arise from surface defects, require large supercell calculations. We use the virtual crystal approximation to introduce fractional defects, and hence 2DEGs, to single unit cells of PTO thin films and PTO/STO superlattices. These simulations will allow us to understand the effect of the 2DEG in ferroelectric materials and will also pave the way for larger calculations with real defects and domains. Using the relaxed geometries from the single unit cell calculations avoids the need to perform geometry relaxations of large supercells, which would be extremely time consuming.

1.3 Landau Theory of Ferroelectrics

Many ferroelectric materials are well-described by a Landau theory: a macroscopic theory in which the free energy is expanded in terms of relevant thermodynamic quantities such as temperature, polarisation, electric field, and strain, etc. The behaviour of the materials can then be determined by minimising the free energy with respect to these quantities. A Landau theory can also be used to study phase transitions in materials. As an example, let us consider the free energy of an ideal ferroelectric perovskite associated with its polarisation and applied electric field. Using a few simple assumptions and symmetry arguments, we will see that the Landau theory describes the paraelectric-ferroelectric phase transition, hysteresis,

and the effect of the depolarising field very well. The free energy can be described in terms of an order parameter, δ, which consists of a soft mode associated with the collective shift of the oxygen cage with respect to the cations, and hence the distortion of the layers. There is a polarisation associated with this mode which can also be used to describe the free energy,

$$P_\delta = \frac{1}{\Omega} Z^*_\delta \delta \,, \tag{1.5}$$

where Ω is the volume of the primitive unit cell and Z^*_δ is the Born effective charge associated with the mode. Due to the symmetry of the perovskite unit cell, we can write the free energy associated with the polarisation as a power series which contains only even powers of P_δ,

$$U_0(P_\delta) = \frac{a}{2} P_\delta^2 + \frac{b}{4} P_\delta^4 + O(P_\delta^6) \,, \tag{1.6}$$

where we truncate the series after the quartic term. Here we consider second order (continuous) phase transitions, where $b \geq 0$. If the quadratic term is positive, then the energy curve will have a single-well-type shape, corresponding to the paraelectric phase. If it is negative, the energy will have a double-well-type shape, corresponding to the ferroelectric phase. Since we know that the ferroelectric phase occurs below a certain Curie temperature, we can assume that $a > 0$ and rewrite (1.6) as

$$U_0(P_\delta) = \frac{a}{2}(T - T_C) P_\delta^2 + \frac{b}{4} P_\delta^4 \,. \tag{1.7}$$

If the temperature is greater than T_C, then both coefficients will be positive, and the energy will have a single-well form with a single minimum at $P_\delta = 0$, i.e. the paraelectric phase is favourable. If the temperature is less than T_C, the energy will have a double-well form with three equilibrium points: an unstable local maximum at $P_\delta = 0$ (paraelectric), and two stable minima at $\pm P_S$, say, the spontaneous polarisation (see Figure 1.3). We can determine P_S by minimising the energy, $\partial_P U_0(P) = 0$:

$$P_S = \left[\frac{a}{b} (T_C - T) \right]^{1/2} \,, \tag{1.8}$$

and defining

$$\varepsilon_0 \chi_\eta = \frac{1}{2a(T_C - T)} \,, \tag{1.9}$$

we can write (1.7) as

$$U_0(P_\delta) = \frac{1}{\varepsilon_0 \chi_\eta} \left(\frac{1}{4} \frac{P_\delta^4}{P_S^2} - \frac{1}{2} P_\delta^2 \right) \,, \tag{1.10}$$

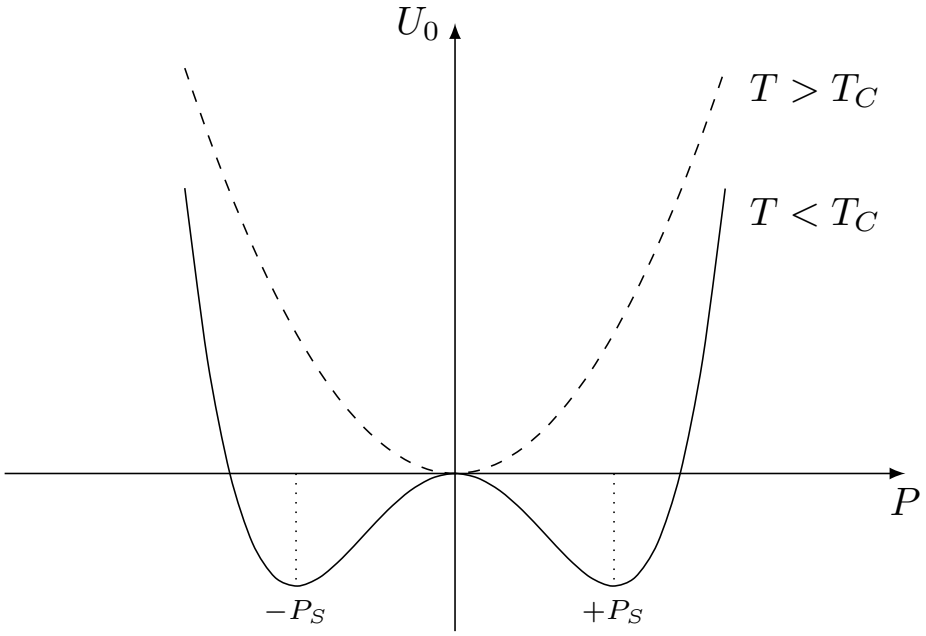

Fig. 1.3 The typical energy curve of an ideal ferroelectric material. The dashed line is the energy curve of the paraelectric phase, the only minimum being at zero polarisation. The black line is the energy of ferroelectric phase, with two minima at $\pm P_S$, the spontaneous polarisation, and a local maximum at zero polarisation.

where χ_η describes the curvature of the energy near the minima.

The application of an external electric field $\vec{E}$ contributes a term to the energy which is proportional to $-\vec{E} \cdot \vec{P}$. This term is linear in the polarisation and has the effect of tilting the wells, making one more favourable than the other. Using this, the hysteresis of the polarisation can be explained using the Landau theory. Applying an external electric field lowers one of the wells, and the system will move towards the minimum of that well. The polarisation will increase until it reaches the bottom of that well, where it saturates at P_S. Reversing the electric field tilts the wells in the opposite direction, and the polarisation will saturate at the bottom of the other well at $-P_S$. In an ideal ferroelectric, this process can be repeated indefinitely resulting in the hysteresis loop shown in Figure 1.4.

Finally, we can use the Landau theory to describe the effect of the depolarising field on ferroelectrics. As we have seen, the depolarising field has an associated energy which is positive and quadratic in the polarisation. For a material to be in the ferroelectric phase, the quadratic term in the free energy must be negative to give the double-well-type shape. The addition of a positive quadratic term from the depolarising field reduces the overall

quadratic coefficient, and thus the energy curve approaches a single-well-type shape, i.e. the ferroelectricity is reduced and the paraelectric phase becomes favoured. In computational simulations of ferroelectric materials, we typically see a small remnant polarisation and a weak depolarising field rather than the material in its paraelectric phase. This is due to the competition between the spontaneous polarisation and the depolarising field: the depolarising field is proportional to the polarisation, and as the polarisation is reduced, so is the depolarising field; both of these quantities decrease iteratively, but are not fully eliminated.

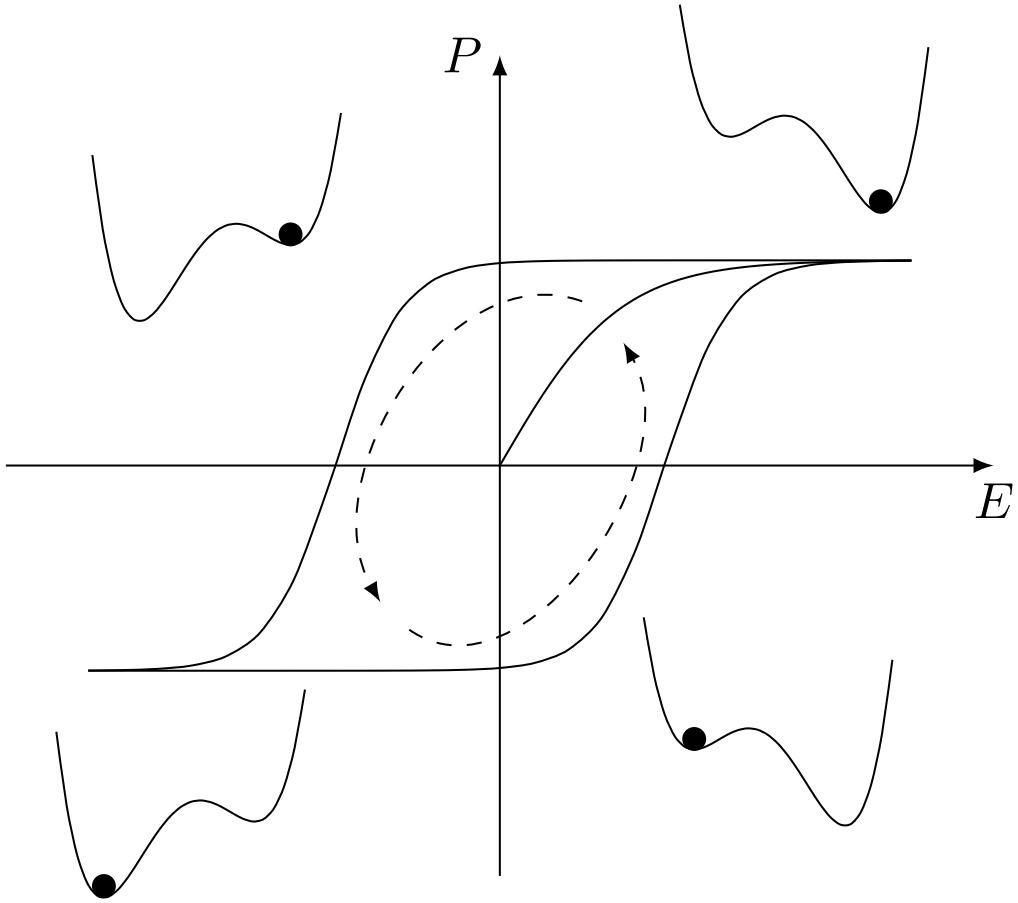

Fig. 1.4 The hysteresis loop of an ideal ferroelectric. The double wells show the free energy of the system in each quadrant. After the initial saturation from zero net polarisation, the external electric field is applied and reversed in an anti-clockwise fashion.

This is the Landau theory of bulk ferroelectrics. For thin films and superlattices, there are additional quantities on which the energy depends, such as the thickness of the films and layers, the width of the ferroelectric domains and the surface charges at the interfaces associated with the 2DEGs. These quantities all contribute to the free energy in different ways,

but the expressions will not be derived here. They are related to the screening mechanisms that arise in the materials, and solving the Landau theory will allow us to determine the behaviour of the screening mechanisms, including their competition and coexistence.

1.4 Screening Mechanisms

2DEGs have been studied both theoretically using a Landau theory approach and computationally using first-principles calculations [14, 15]. They are typically observed in monodomain phases. We should note here that 2DEGs can have different physical origins in different materials. In some materials, such as LAO/STO superlattices, the 2DEG arises due to an intrinsic polar discontinuity at the interfaces in order to prevent a polar catastrophe [16]. In materials such as PTO/STO superlattices, a 2DEG can arise due to surface or interfacial defects, namely oxygen and cation vacancies. If we employ a Landau theory to model the ferroelectrics as a function of thin film thickness, we find that the screening method observed depends on the thickness of the film. For thinner films, domains dominate, and when the width of the domains, w, is less than the thickness, d, the Kittel law is obeyed [17],

$$w \propto \sqrt{d}\,. \tag{1.11}$$

The monodomain limit is obtained when the width of the domains tends to infinity. In this limit, the domains vanish and the 2DEG dominates as the screening mechanism. It was recently suggested in [14] that there is a transition between the screening mechanism favoured which depends on the thickness of the film. This can be seen by analysing the free energies of both scenarios. Figure 1.5 shows a comparison of the energies of the monodomain and polydomain configurations of PTO. From the plot we see that for thinner films, a polydomain configuration is preferable, and for thicker films, a monodomain configuration with a 2DEG is preferred. There is a crossover length, $d_{\mathrm{co}} \approx 4.6$ nm, beyond which the favoured screening mechanism changes. This analysis suggests that there is a sharp change of the preferred screening mechanism, but does not allow for the possibility of observing both ferroelectric domains and 2DEGs simultaneously.

1.4.1 Coexistence

Recently, a model of coexistence between domains and 2DEGs was proposed for a ferroelectric thin film in a vacuum [18]. By modifying the Landau theory for a thin film broken into domains to account for the presence of 2DEGs at the surfaces, analytic and numerical

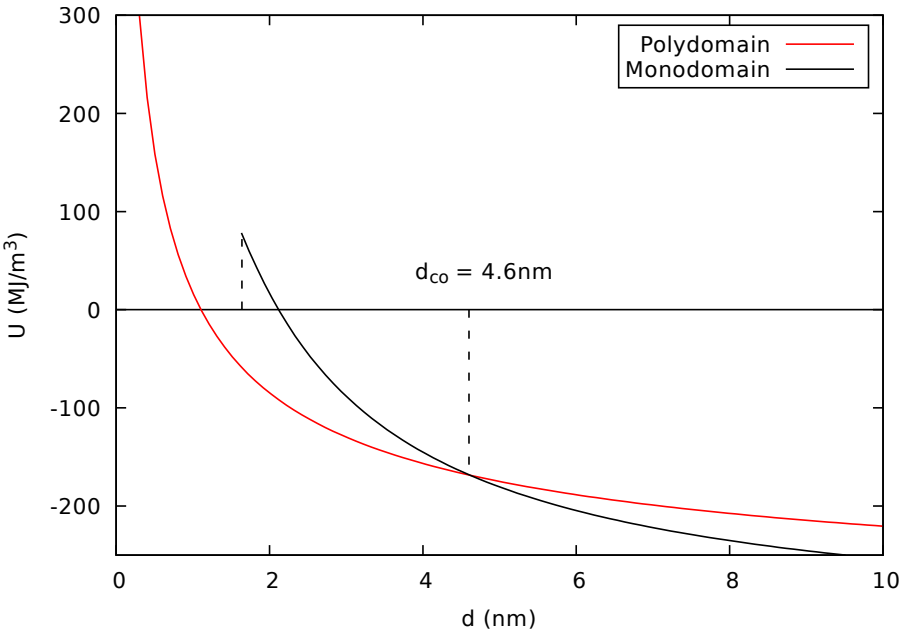

Fig. 1.5 A comparison of the free energies of the monodomain and polydomain states thin films of PTO as a function of thickness. The crossover length is d_{co}. Zero energy corresponds to the paraelectric phase. Details of the calculation of these energies can be found in [14].

approximations were used to solve the theory and study the behaviour of the screening mechanisms. The work suggests that instead of a sharp crossover from one screening mechanism to the other as indicated in Figure 1.5, there is actually a smooth transition from one to the other, with a region of coexistence in between.

The results of this theory are summarised in Figure 1.6 for a thin film of PTO. We see that below a critical thickness, d_c, there is no 2DEG and the domains obey the Kittel law. There is a thickness, d_p, at which the width of the domains diverge and the surface charge saturates to the spontaneous polarisation, completely screening the depolarising field. The coexistence region is between d_c and d_p, and in this region we see that there is both a 2DEG which is not fully saturated and domains which do not obey the Kittel law, but have finite width.

This theory suggests an interesting relationship between the screening mechanisms, but only in the ideal case of a thin film in a vacuum. Experimentally, ferroelectric thin films are grown on substrates: PTO is typically grown on a substrate of STO. Ferroelectrics are also typically grown in superlattices with alternating layers in order to optimise the technological properties of the constituent materials; a common example is a superlattice of alternating layers of ferroelectric PTO and paraelectric STO. The previous theory of coexistence describes a

thin film in a vacuum but does not describe thin films on substrates or superlattices. In the aforementioned examples, the dielectric constant of STO can be orders of magnitude larger than those of PTO [19]. While the theory describes coexistence of the screening mechanisms of an individual thin film, it does not account for the influence that its environment may have on the range and nature of coexistence.

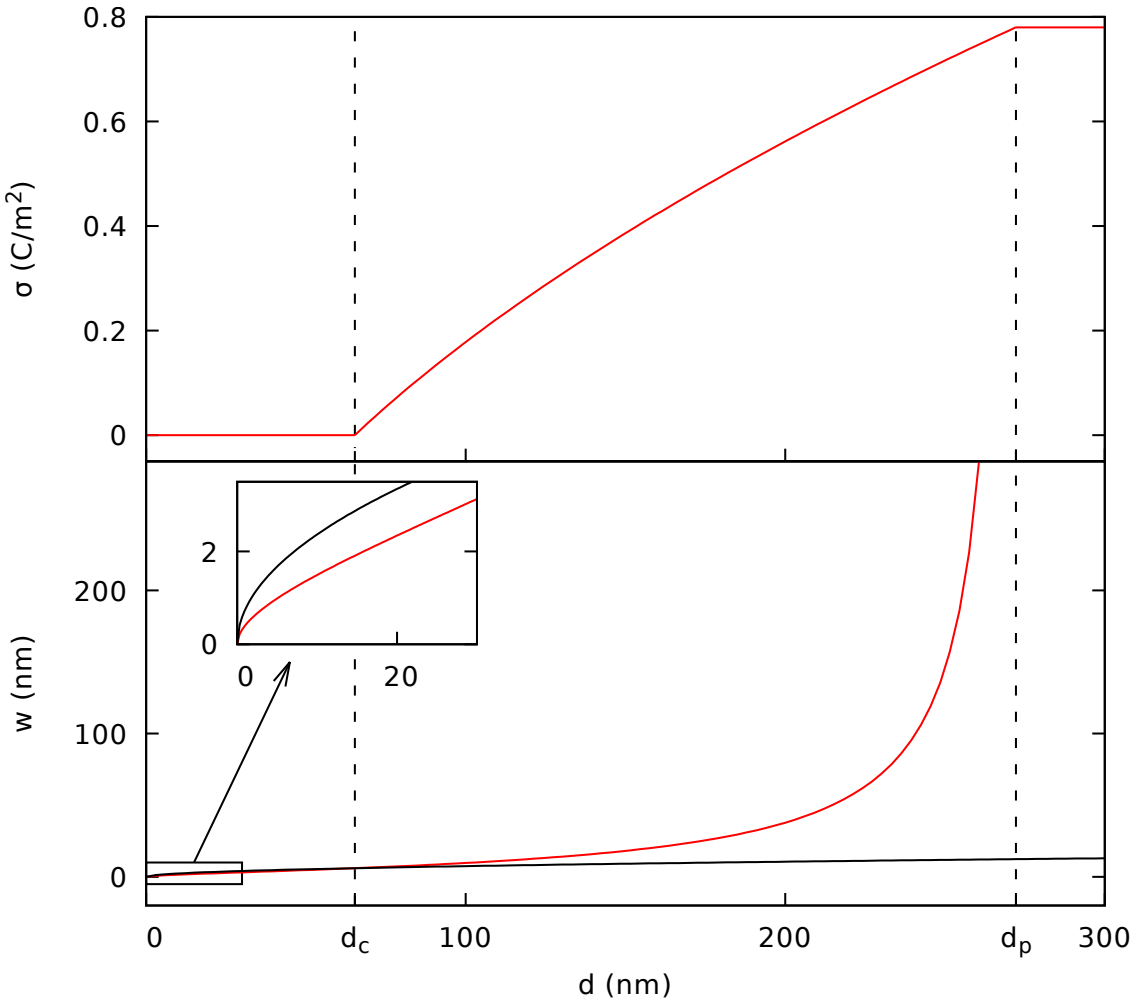

Fig. 1.6 Results of the coexistence model for a thin film of PTO. The red curves show the 2DEG surface charge, σ, and the domain widths, w, as a function of thickness, d. The black curve in the lower plot shows the Kittel law for for the same film without a 2DEG. We see that below the critical thickness, there is no 2DEG and the domains obey the Kittel law. Above d_p, the domain widths diverge and the 2DEG surface charge saturates at the spontaneous polarisation. Between these thicknesses there is both a nonzero surface charge and a finite domain width.

Chapter 2

Theory

In this chapter we study the electrostatic description of ferroelectric materials with the aim of correctly describing the effects of a substrate and superlattice geometry on the system. Having done this, we can update the Landau theories and study the screening mechanisms in more realistic situations. First, we review the theory for a thin film in a vacuum carefully as it is not derived in detail in the literature. We then make the necessary modifications to describe substrates and superlattices.

2.1 Electrostatics

For a ferroelectric thin film in a vacuum, we follow the derivation and nomenclature used in [13]. Consider a ferroelectric thin film in a vacuum of thickness d which is infinitely wide and is saturated at its spontaneous polarisation P_S. The thin film is broken into a repeating pattern of ferroelectric domains of equal and opposite polarisation, as shown in Figure 2.1. We assume the walls between the domains to be infinitely thin. Note that this is a two-dimensional model, and we seemingly ignore the width in the y-direction. In reality, the domains are very long in this direction. We think of the material as infinitely wide in this direction, and describe a cross-section at a fixed value of y.

The spontaneous polarisation inside the thin film is periodic in x, with period $W = W_+ + W_-$. We choose the origin of our coordinate system such that it is an even function of x. Thus, we can represent the spontaneous polarisation as a Fourier series,

$$P_S(x) = AP_S + \sum_{n=1}^{\infty} \frac{4P_S}{n\pi} \sin\left(\frac{n\pi}{2}(A+1)\right) \cos(nkx) \,, \tag{2.1}$$

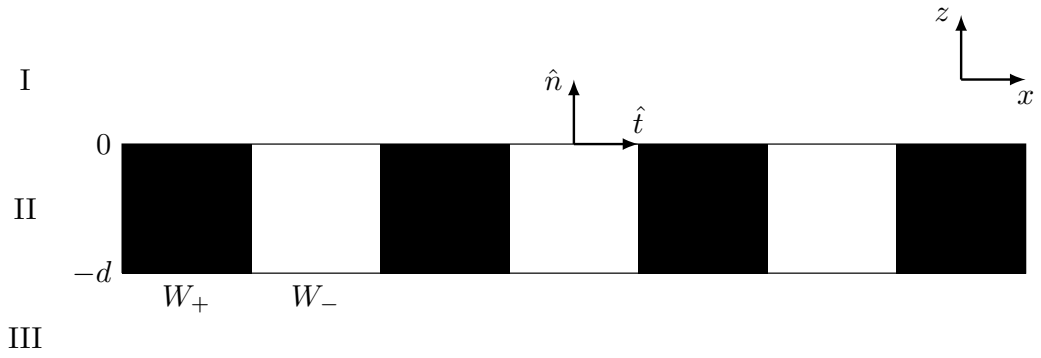

Fig. 2.1 A ferroelectric thin film in a vacuum, broken into domains. The black regions represent domains with polarisation $+P_S$ and width W_+, and the white regions represent domains with polarisation $-P_S$ and width W_-.

where

$$A = \frac{W_+ - W_-}{W_+ + W_-} \tag{2.2}$$

is the mismatch between the domain widths, and

$$k = \frac{2\pi}{W} \,. \tag{2.3}$$

The polydomain (Kittel) limit is obtained when $A \to 0$, i.e. the domain widths are equal. The monodomain limit is obtained when $A \to \pm 1$, i.e. one of the domain widths tends to zero. To obtain the electric fields inside and outside of the film, we must first determine the electrostatic potentials. They satisfy the following Laplace equations

$$\begin{aligned} \kappa_{ij}\partial_i\partial_j\phi_{\mathrm{II}} &= 0 \\ \nabla^2\phi_{\mathrm{I}} = \nabla^2\phi_{\mathrm{III}} &= 0 \end{aligned} \,, \tag{2.4}$$

where $\kappa = \begin{bmatrix} \kappa_a & 0 \\ 0 & \kappa_c \end{bmatrix}$ is the permittivity tensor of the thin film. The general solutions are of the form

$$\begin{aligned}
\phi_{\mathrm{I}}(x,z) &= \sum_{n=1}^{\infty}\left(a_n^1 e^{in\lambda_1 x}+b_n^1 e^{-in\lambda_1 x}\right)\left(c_n^1 e^{n\lambda_1 z}+d_n^1 e^{-n\lambda_1 z}\right)+a_0^1(z)\\
\phi_{\mathrm{II}}(x,z) &= \sum_{n=1}^{\infty}\left(a_n^2 e^{in(\lambda_2/\sqrt{\kappa_a})x}+b_n^2 e^{-in(\lambda_2/\sqrt{\kappa_a})x}\right)\left(c_n^2 e^{n(\lambda_2/\sqrt{\kappa_c})z}+d_n^2 e^{-n(\lambda_2/\sqrt{\kappa_c})z}\right)+a_0^2(z)\,. \qquad (2.5)\\
\phi_{\mathrm{III}}(x,z) &= \sum_{n=1}^{\infty}\left(a_n^3 e^{in\lambda_3 x}+b_n^3 e^{-in\lambda_3 x}\right)\left(c_n^3 e^{n\lambda_3 z}+d_n^3 e^{-n\lambda_3 z}\right)+a_0^3(z)
\end{aligned}$$

Since the potentials must be even and periodic in x, they reduce to

$$\begin{aligned}
\phi_{\mathrm{I}}(x,z) &= \sum_{n=1}^{\infty}\cos(nkx)\left(c_n^1 e^{nkz}+d_n^1 e^{-nkz}\right)+a_0^1(z)\\
\phi_{\mathrm{II}}(x,z) &= \sum_{n=1}^{\infty}\cos(nkx)\left(c_n^2 e^{nkcz}+d_n^2 e^{-nkcz}\right)+a_0^2(z)\,, \qquad (2.6)\\
\phi_{\mathrm{III}}(x,z) &= \sum_{n=1}^{\infty}\cos(nkx)\left(c_n^3 e^{nkz}+d_n^3 e^{-nkz}\right)+a_0^3(z)
\end{aligned}$$

where the coefficients a_n^i have been absorbed into the other coefficients, and

$$c=\sqrt{\frac{\kappa_a}{\kappa_c}}\,. \qquad (2.7)$$

Excluding the $n=0$ terms, which can be dealt with separately because all terms are linearly independent, we require 6 conditions to determine the 6 remaining coefficients. We state our assumptions here clearly as it will become important to keep track of them when we generalise to a less symmetric case:

- The fields in the vacuum regions must vanish at $\pm\infty$:

$$c_n^1 = d_n^3 = 0\,. \qquad (2.8)$$

- The fields must be equal at the interfaces between the thin film and vacuum regions:

$$\begin{aligned}
\phi_{\mathrm{I}}(x,0) &= \phi_{\mathrm{II}}(x,0)\\
\phi_{\mathrm{III}}(x,-d) &= \phi_{\mathrm{II}}(x,-d)
\end{aligned}\,. \qquad (2.9)$$

- The components of the displacement fields normal to the interfaces of the thin film must be equal at the interfaces, providing the final two constraints:

$$(\vec{D}_{\mathrm{I}} - \vec{D}_{\mathrm{II}}) \cdot \hat{n} = (\vec{D}_{\mathrm{III}} - \vec{D}_{\mathrm{II}}) \cdot \hat{n} = 0 \,, \tag{2.10}$$

  where $\hat{n}$ is a unit vector normal to the surface. The displacement fields are given by

$$\begin{aligned} \vec{D}_{\mathrm{I}} &= \varepsilon_0 \vec{E}_{\mathrm{I}} \\ \vec{D}_{\mathrm{II}} &= \varepsilon_0 \kappa \vec{E}_{\mathrm{II}} + \vec{P}_S \,, \\ \vec{D}_{\mathrm{III}} &= \varepsilon_0 \vec{E}_{\mathrm{III}} \end{aligned} \tag{2.11}$$

  and using $\vec{E} = -\vec{\nabla}\phi$, we get

$$\begin{aligned} \kappa_c \partial_z \phi_{\mathrm{II}}|_{z=0} - \partial_z \phi_{\mathrm{I}}|_{z=0} &= \frac{1}{\varepsilon_0} P_S(x,0) \\ \kappa_c \partial_z \phi_{\mathrm{II}}|_{z=-d} - \partial_z \phi_{\mathrm{III}}|_{z=-d} &= \frac{1}{\varepsilon_0} P_S(x,-d) \end{aligned} \,. \tag{2.12}$$

We use the third condition to determine the $n = 0$ terms separately. Inside the film we have

$$\varepsilon_0 \kappa_c \partial_z a_0^2(z) = A P_S \,, \tag{2.13}$$

which gives

$$a_0^2(z) = \frac{A P_S}{\varepsilon_0 \kappa_c} z \,. \tag{2.14}$$

Equating the $n = 0$ terms at the interfaces gives

$$\begin{aligned} a_0^1 &= 0 \\ a_0^3 &= -\frac{A P_S}{\varepsilon_0 \kappa_c} d \end{aligned} \,. \tag{2.15}$$

This resembles the potential for a monodomain thin film with polarisation AP_S. Using this and the first condition, the potentials simplify to

$$\begin{aligned}\phi_{\mathrm{I}}(x,z) &= \sum_{n=1}^{\infty} d_n^1 \cos(nkx) e^{-nkz} \\ \phi_{\mathrm{II}}(x,z) &= \frac{AP_S}{\varepsilon_0 \kappa_c} z + \sum_{n=1}^{\infty} \cos(nkx) \left(c_n^2 e^{nkcz} + d_n^2 e^{-nkcz} \right) . \\ \phi_{\mathrm{III}}(x,z) &= -\frac{AP_S}{\varepsilon_0 \kappa_c} d + \sum_{n=1}^{\infty} c_n^3 \cos(nkx) e^{nkz}\end{aligned} \tag{2.16}$$

Using the second condition and matching the potentials at the interfaces yields

$$\begin{aligned} d_n^1 &= \left(c_n^2 + d_n^2 \right) \\ c_n^3 e^{-nkd} &= \left(c_n^2 e^{-2nR} + d_n^2 e^{2nR} \right) \end{aligned} , \tag{2.17}$$

where

$$R = \frac{\pi cd}{W} , \tag{2.18}$$

so that

$$kcd = 2R . \tag{2.19}$$

Using the third condition to match the displacement fields at the interfaces yields

$$\begin{aligned} \kappa_c (nkc) \left(c_n^2 + d_n^2 \right) - (-nk) d_n^1 &= \frac{1}{\varepsilon_0} \frac{4P_S}{n\pi} \sin\left(\frac{n\pi}{2} (A+1) \right) \\ \kappa_c (nkc) \left(c_n^2 e^{-2nR} + d_n^2 e^{2nR} \right) - (nk) c_n^3 e^{-nkd} &= \frac{1}{\varepsilon_0} \frac{4P_S}{n\pi} \sin\left(\frac{n\pi}{2} (A+1) \right) \end{aligned} . \tag{2.20}$$

Combining this with (2.17) we get

$$d_n^2 = -c_n^2 e^{-2nR} , \tag{2.21}$$

and thus, the potential inside the film simplifies to

$$\phi_{\mathrm{II}}(x,z) = \frac{AP_S}{\varepsilon_0 \kappa_c} z + \sum_{n=1}^{\infty} c_n^2 \cos(nkx) \sinh(nR + cnkz) , \tag{2.22}$$

meaning first part of (2.9) simplifies to

$$a_n^1 d_n^1 = a_n^2 c_n^2 e^{-nR} \sinh(nR) \,. \tag{2.23}$$

This simplifies (2.17) and (2.20):

$$\begin{aligned} d_n^1 &= c_n^2 \sinh(nR) \\ c_n^3 e^{-nkd} &= -c_n^2 \sinh(nR) \end{aligned}, \tag{2.24}$$

giving

$$\begin{aligned} c_n^2 \left(g\cosh(nR) + \sinh(nR)\right) &= \frac{4P_S}{n^2\pi k} \sin\left(\frac{n\pi}{2}(A+1)\right) \\ \implies c_n^2 &= \frac{4P_S}{n^2\pi k} \sin\left(\frac{n\pi}{2}(A+1)\right) \frac{1}{\sinh(nR) + g\cosh(nR)} \end{aligned}, \tag{2.25}$$

where

$$g = \sqrt{\kappa_a \kappa_c} = c\kappa_c \,. \tag{2.26}$$

Finally, the potentials are given by

$$\begin{aligned} \phi_{\mathrm{I}}(x,z) &= \frac{1}{4\pi\varepsilon_0} \sum_{n=1}^{\infty} \frac{1}{n^2} \frac{8P_S cd}{R} \sin\left(\frac{n\pi}{2}(A+1)\right) \cos(nkx) \frac{e^{-nkz}}{1+g\coth(nR)} \\ \phi_{\mathrm{II}}(x,z) &= \frac{AP_S}{\varepsilon_0\kappa_c} z + \frac{1}{4\pi\varepsilon_0} \sum_{n=1}^{\infty} \frac{1}{n^2} \frac{8P_S cd}{R} \sin\left(\frac{n\pi}{2}(A+1)\right) \cos(nkx) \frac{\sinh(nR+cnkz)}{\sinh(nR)+g\cosh(nR)} \,. \\ \phi_{\mathrm{III}}(x,z) &= -\frac{AP_S}{\varepsilon_0\kappa_c} d - \frac{1}{4\pi\varepsilon_0} \sum_{n=1}^{\infty} \frac{1}{n^2} \frac{8P_S cd}{R} \sin\left(\frac{n\pi}{2}(A+1)\right) \cos(nkx) \frac{e^{nk(z+d)}}{1+g\coth(nR)} \end{aligned} \tag{2.27}$$

The depolarisation energy *per unit area* is the sum of contributions from each of the three regions,

$$\begin{aligned} U_{\mathrm{I,III}} &= \int \frac{1}{2} \left(E_x^2 + E_z^2\right) \mathrm{d}x\,\mathrm{d}z \\ U_{\mathrm{II}} &= \int \frac{1}{2} \left(\kappa_a E_x^2 + \kappa_c E_z^2\right) \mathrm{d}x\,\mathrm{d}z \end{aligned} \,. \tag{2.28}$$

For the integration in the x-direction, we average over the domain period. To simplify the integration, we introduce the following notation:

$$\begin{aligned}\alpha &= \frac{1}{4\pi\varepsilon_0}\left(\frac{8P_S cd}{R}\right)\\ \beta_n &= \frac{1}{\sinh(nR)+g\cosh(nR)}\\ \gamma_n &= \frac{1}{1+g\coth(nR)}\end{aligned}\quad . \tag{2.29}$$

Then the electric fields in region II are given by

$$\begin{aligned}E_z &= -\frac{AP_S}{\varepsilon_0\kappa_c} - \alpha kc\sum_{n=1}^{\infty}\frac{\sin\left(\frac{n\pi}{2}(A+1)\right)}{n}\cos(nkx)\beta_n\cosh(nR+nkcz)\\ E_x &= \alpha k\sum_{n=1}^{\infty}\frac{\sin\left(\frac{n\pi}{2}(A+1)\right)}{n}\sin(nkx)\beta_n\sinh(nR+nkcz)\end{aligned}\quad . \tag{2.30}$$

When we square E_z, we get three terms, but the cross term vanishes when integrated over a period in the x-direction. The first part of E_z, the monodomain part, contributes the following to the depolarising energy:

$$U_{\text{mono}} = \frac{1}{2}\varepsilon_0\kappa_c\int_{-d}^{0}\frac{1}{W}\int_{-W/2}^{W/2}\mathrm{d}z\,\mathrm{d}x\left(\frac{AP_S}{\varepsilon_0\kappa_c}\right)^2 = \frac{1}{2}\frac{P_S^2 d}{\varepsilon_0\kappa_c}A^2\,. \tag{2.31}$$

For the remaining terms, we make use of the orthogonality relations to perform the integration in the x-direction,

$$\frac{1}{W}\int_{-W/2}^{W/2}\cos(nkx)\cos(mkx)\,\mathrm{d}x = \frac{1}{W}\int_{-W/2}^{W/2}\sin(nkx)\sin(mkx)\,\mathrm{d}x = \frac{1}{2}\delta_{nm}\,, \tag{2.32}$$

so the rest of the depolarising energy simplifies to

$$U_{\text{II}} = \frac{1}{2}\frac{P_S^2 d}{\varepsilon_0\kappa_c}\frac{8g}{\pi^2 R}\sum_{n=1}^{\infty}\frac{\sin^2\left(\frac{n\pi}{2}(A+1)\right)}{n^3}\gamma_n^2 g\coth(nR)\,. \tag{2.33}$$

Similarly for regions I and II, we get

$$U_{\text{I,III}} = \frac{1}{4}\frac{P_S^2 d}{\varepsilon_0\kappa_c}\frac{8g}{\pi^2 R}\sum_{n=1}^{\infty}\frac{\sin^2\left(\frac{n\pi}{2}(A+1)\right)}{n^3}\gamma_n^2\,. \tag{2.34}$$

Adding the three of these together, along with the monodomain part of the energy in region II, we get

$$U_{\text{dep}} = \frac{1}{2}\frac{P_S^2 d}{\varepsilon_0 \kappa_c}\left(A^2 + \frac{8g}{\pi^2 R}\sum_{n=1}^{\infty}\frac{\sin^2\left(\frac{n\pi}{2}(A+1)\right)}{n^3}\frac{1}{(1+g\coth(nR))}\right) . \tag{2.35}$$

This is the depolarising energy *per unit area*.

Let us analyse the form of this potential and check that it has the correct behaviour in the monodomain and Kittel limits. First, set the domain widths to be equal, $W_+ = W_- = w$, such that $W = 2w$ and $A = 0$. Next, we divide by d to obtain the energy *per unit volume* (of the thin film). Under these assumptions, the energy simplifies to

$$U_{\text{dep}} = \frac{1}{2}\frac{P_S^2}{\varepsilon_0 \kappa_c}\left(\frac{8g}{\pi^2 R}\sum_{n=1}^{\infty}\frac{1}{n^3}\sin^2\left(\frac{n\pi}{2}\right)\frac{1}{(1+g\coth(nR))}\right) . \tag{2.36}$$

We would like to write this in terms of the ratio of the thickness to width, $r = d/w$,

$$U_{\text{dep}} = \frac{P_S^2}{2\varepsilon_0 \kappa_c}\left(\frac{16g}{\pi^3 c}\right)\frac{1}{x}\sum_{n=1}^{\infty}\frac{1}{n^3}\sin^2\left(\frac{n\pi}{2}\right)\frac{1}{\left(1+g\coth\left(\frac{n\pi}{2}cx\right)\right)} , \tag{2.37}$$

and examine the behaviour in the different limits. In monodomain limit, $r \to 0$ ($w \to \infty$), we should obtain

$$U_{\text{mono}} = \frac{1}{2\varepsilon_0 \kappa_c}P_S^2 . \tag{2.38}$$

Evaluating the limit

$$\lim_{r\to 0}\frac{1}{r\left(1+g\coth\left(\frac{n\pi}{2}cr\right)\right)} = \frac{n\pi}{2}\frac{c}{g} , \tag{2.39}$$

we get

$$\lim_{r\to 0} U_{\text{dep}} = \frac{P_S^2}{2\varepsilon_0 \kappa_c}\frac{8}{\pi^2}\sum_{n=1}^{\infty}\frac{1}{n^2}\sin^2\left(\frac{n\pi}{2}\right) . \tag{2.40}$$

The inifinite sum converges to

$$\sum_{n=1}^{\infty}\frac{1}{n^2}\sin^2\left(\frac{n\pi}{2}\right) = \frac{\pi^2}{8} , \tag{2.41}$$

and thus the correct monodomain limit is obtained when $r \to 0$. In the limit $r \gg 1$, a Kittel-like expression should be observed,

$$U_{\text{Kittel}} \propto \frac{1}{r} . \tag{2.42}$$

As we will see in the next section, this is the limit that leads to the Kittel law, (1.11), for ferroic materials. Note that we have already taken the $A \to 0$ limit before taking the $r \gg 1$ limit. Using

$$\lim_{r\to\infty} \coth\left(\frac{n\pi}{2}cr\right) = 1 \,, \tag{2.43}$$

we get

$$\lim_{r\to\infty} U_{\text{dep}} \approx \frac{P_S^2}{2\varepsilon_0}\frac{16}{\pi^3(1+g)}\frac{1}{x}\sum_{n=1}^{\infty}\frac{1}{n^3}\sin^2\left(\frac{n\pi}{2}\right) . \tag{2.44}$$

The infinite series converges to,

$$\sum_{n=1}^{\infty}\frac{1}{n^3}\sin^2\left(\frac{n\pi}{2}\right) = \frac{1}{8}(-2\psi^{(2)}(1)+3\zeta(3)) \approx 1.0518 \,, \tag{2.45}$$

where $\zeta(z)$ is the Riemann Zeta function, and

$$\psi^{(m)}(z) = \frac{d^{m+1}}{dz^{m+1}}\ln(\Gamma(z)) \,, \tag{2.46}$$

is the polygamma function. So we obtain the Kittel expression in the limit $x \to \infty$,

$$\lim_{r\to\infty} U_{\text{dep}}(x) = \frac{P_S^2}{2\varepsilon_0}\beta\frac{1}{r} \,, \tag{2.47}$$

where

$$\beta = \frac{16}{\pi^3(1+g)}\sum_{n=1}^{\infty}\frac{1}{n^2}\sin^2\left(\frac{n\pi}{2}\right) = \frac{16.829\ldots}{\pi^3(1+g)} \,. \tag{2.48}$$

Thus, the full electrostatic description reproduces the correct behaviour in both the monodomain and Kittel limits. Figure 2.2 shows the electrostatic energy as a function of r for a thin film of PTO. In this chapter, we use the parameters from [14] for PTO, which were obtained using first-principles calculations. We see that the energy approaches the monodomain limit as $r \to 0$ and has Kittel-like behaviour when $r > 1$.

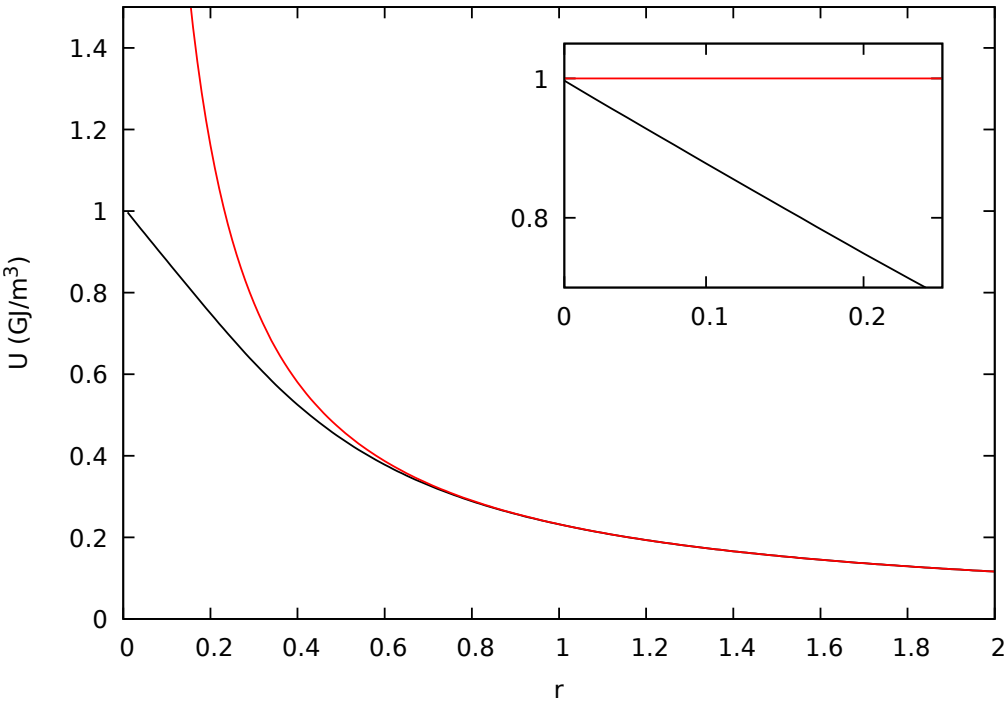

Fig. 2.2 The depolarising energy (black) of a thin film of PTO. The red curve shows the Kittel expression for the same film of PTO. We see that for $r > 1$, the energy follows the Kittel expression. Inset: the depolarising energy in the monodomain limit, $r \to 0$. The horizontal red line shows the monodomain energy of PTO.

2.1.1 Substrate

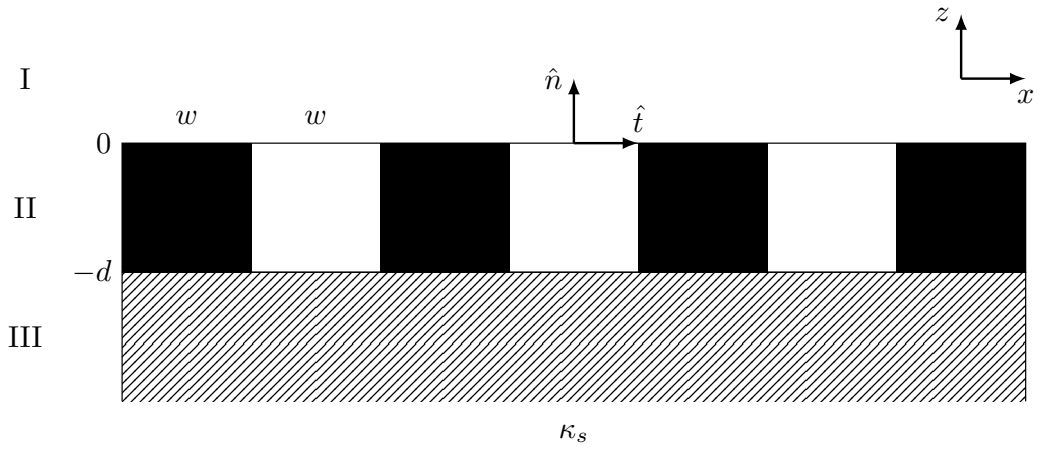

Fig. 2.3 A ferroelectric thin film on a substrate of permittivity κ_s. The substrate is dielectric, isotropic and semi-infinite.

Following the procedure used in the previous section, we consider the electrostatics of a thin film on a substrate. To introduce the substrate, we replace the vacuum in medium III with an isotropic material of permittivity κ_s. The Laplace equation in medium III becomes

$$\kappa_s \nabla^2 \phi_{\mathrm{III}} = 0 \,, \tag{2.49}$$

which is the same as before. Since everything is still even and periodic in x, we start with

$$\begin{aligned}
\phi_{\mathrm{I}}(x,z) &= a_0^1(z) + \sum_{n=1}^{\infty} \cos(nkx) d_n^1 e^{-nkz} \\
\phi_{\mathrm{II}}(x,z) &= a_0^2(z) + \sum_{n=1}^{\infty} \cos(nkx) \left(c_n^2 e^{cnkz} + d_n^2 e^{-cnkz} \right) \,, \\
\phi_{\mathrm{III}}(x,z) &= a_0^3(z) + \sum_{n=1}^{\infty} \cos(nkx) c_n^3 e^{nkz}
\end{aligned} \tag{2.50}$$

for the solutions. For the monodomain case, the potentials were derived irrespective of the permittivities of the media on either side of the thin film. Thus, we expect the monodomain limit to be unaffected by the presence of the substrate. If we treat the $n = 0$ terms in the same way as before, we find that they are exactly the same as (2.14) and (2.15), as expected. For the $n \neq 0$ terms, we use the same constraints to fix the remaining coefficients. Matching the potentials at the interface gives

$$\begin{aligned} d_n^1 &= \left(c_n^2 + d_n^2\right) \\ c_n^3 e^{-nkd} &= \left(c_n^2 e^{-2nR} + d_n^2 e^{2nR}\right) \end{aligned} . \tag{2.51}$$

The displacement field in region III now has an additional factor of κ_s,

$$\vec{D}_{\mathrm{III}} = \varepsilon_0 \kappa_s \vec{E}_{\mathrm{III}} \tag{2.52}$$

Thus, we need to modify all of the boundary conditions that involve the displacement fields. In this case, (2.21) is replaced by

$$d_n^2 = -e^{-2nR}\left(\frac{2g\sinh(nR) + (e^{nR} + \kappa_s e^{-nR})}{2g\sinh(nR) + (\kappa_s e^{nR} + e^{-nR})}\right) c_n^2 . \tag{2.53}$$

It is important to note that at every step in this derivation, the vacuum limit should be obtained when $\kappa_s \to 1$. Here we see that in the limit $\kappa_s \to 1$, (2.21) is indeed obtained. After a bit of algebra, the potential in the thin film can be written as

$$\begin{aligned} \phi_{\mathrm{II}}(x,z) = \sum_{n=1}^{\infty} c_n^2 \cos(knx) \,(2g\sinh(nR)\sinh(nkcz + nR) + \\ + \sinh(nkcz) + \kappa_s \sinh(nkcz + 2nR)) \end{aligned} . \tag{2.54}$$

In the limit $\kappa_s \to 1$, it becomes proportional to $\sinh(nkcz + nR)$ as in the vacuum case. Returning to the displacement field conditions, we get

$$c_n^2 = \alpha \frac{1}{n^2} \sin\left(\frac{n\pi}{2}(A+1)\right) \gamma_n , \tag{2.55}$$

where α is as defined in the previous section and

$$\gamma_n = \left[(\kappa_s + g^2)\sinh(2nR) + g\left(1 + \kappa_s \cosh(2nR) + 2\sinh^2(nR)\right)\right]^{-1} . \tag{2.56}$$

Matching the potentials at the interfaces again gives

$$\begin{aligned} d_n^1 &= \left[2g\sinh^2(nR) + \kappa_s \sinh(2nR)\right] c_n^2 \\ c_n^3 &= -e^{nkd}\left[2g\sinh^2(nR) + \sinh(2nR)\right] c_n^2 \end{aligned} . \tag{2.57}$$

So finally, we get

$$\begin{aligned}
\phi_{\mathrm{I}}(x,z) &= 0+\alpha\sum_{n=1}^{\infty}\frac{1}{n^2}\sin\left(\frac{n\pi}{2}(A+1)\right)\cos(nkx)e^{-nkz}\gamma_n\left[2g\sinh^2(nR)+\kappa_s\sinh(2nR)\right]\\
\phi_{\mathrm{II}}(x,z) &= \frac{AP_S}{\varepsilon_0\kappa_c}z+\alpha\sum_{n=1}^{\infty}\frac{1}{n^2}\sin\left(\frac{n\pi}{2}(A+1)\right)\cos(nkx)\gamma_n\left[2g\sinh(nR)\sinh(nkcz+nR)\right.\\
&\qquad\left.+\sinh(nkcz)+\kappa_s\sinh(nkcz+2nR)\right]\\
\phi_{\mathrm{III}}(x,z) &= -\frac{AP_S}{\varepsilon_0\kappa_c}d-\alpha\sum_{n=1}^{\infty}\frac{1}{n^2}\sin\left(\frac{n\pi}{2}(A+1)\right)\cos(nkx)e^{nk(z+d)}\gamma_n\left[2g\sinh^2(nR)+\sinh(2nR)\right]
\end{aligned}\tag{2.58}$$

These potentials all reduce to the expressions obtained for the vacuum case in the limit $\kappa_s \to 1$. For the depolarising energy, we integrate the electric fields as before, the only difference being that the energy in the substrate is scaled by a factor of κ_s. After some integration, the depolarising energy *per unit area* is found to be

$$\begin{aligned}
U_{\mathrm{dep}} = \frac{1}{2}\frac{P_S^2 d}{\varepsilon_0\kappa_c}\Bigg[A^2+\frac{4g}{\pi^2 R}\sum_{n=1}^{\infty}\frac{1}{n^3}\sin^2\left(\frac{n\pi}{2}(A+1)\right)\gamma_n^2\Big(4g\sinh(2nR)\left(\cosh(nR)+g\sinh(nR)\right)^2\\
\times\left(2g\sinh^2(nR)+\kappa_s\sinh(2nR)\right)^2+\kappa_s\left(2g\sinh^2(nR)+\sinh(2nR)\right)^2\Big)\Bigg]
\end{aligned}\tag{2.59}$$

which looks messy, but does reproduce the vacuum case when $\kappa_s \to 1$.

Next, we analyse the behaviour of the energy in the monodomain and polydomain limits as before. We expect the monodomain limit to be exactly the same as the vacuum case, and the polydomain limit to display Kittel-like behaviour. It was initially found that the vacuum case was not reproduced in the monodomain limit. The reason for this was that in the vacuum case we let $A \to 0$ before using $r = d/w$ to take the monodomain and polydomain limits. The fact that the correct monodomain limit for the thin film in a vacuum was obtained is just an anomaly of the symmetric coordinate system used; it was centred in the middle of one of the domains. Fixing the widths to be equal and sending $w \to \infty$ still reproduced the monodomain limit. In general, it appears that the limits $A \to 0$ and $w \to \infty$ do not commute; the presence of the substrate seems to break the symmetry that made these limits interchangeable in the vacuum case. In order to correctly take the monodomain limit, we should let $A \to 1$, i.e. the width of one type of domain tends to zero. In this limit, the $n \neq 0$ terms vanish automatically as $\sin(n\pi) = 0$ for $n \in \mathbb{Z}$, and the monodain expression is obtained immediately. It is exactly

the same as the vacuum case, as expected.

Having dealt with the monodomain limit correctly, we let $A \to 0$ to investigate the polydomain limit. We write the energy *per unit volume* as a function of r and take the limit $r \to \infty$ and get

$$\lim_{r\to\infty} U_{\text{dep}}(x) \approx \frac{P_S^2}{2\varepsilon_0}\beta(\kappa_s)\frac{1}{r}\,, \tag{2.60}$$

where

$$\beta(\kappa_s) = \frac{8}{\pi^3}\left[\frac{1}{(1+g)^2} + \frac{2g+\kappa_s}{(g+\kappa_s)^2}\right]\sum_{n=1}^{\infty}\frac{1}{n^3}\sin^2\left(\frac{n\pi}{2}\right)\,. \tag{2.61}$$

This converges to (2.48) when $\kappa_s \to 1$. This is an important result as it implies that when we move away from the ideal case of a thin film in a vacuum, the Kittel law is still obeyed. Using the constant $\beta(\kappa_s)$, we can investigate how the permittivity of the substrate affects the behaviour of the domains. This analysis can also be used to investigate the effect of the substrate on the coexistence of screening mechanisms, as we will see in the next section.

2.1.2 Superlattice

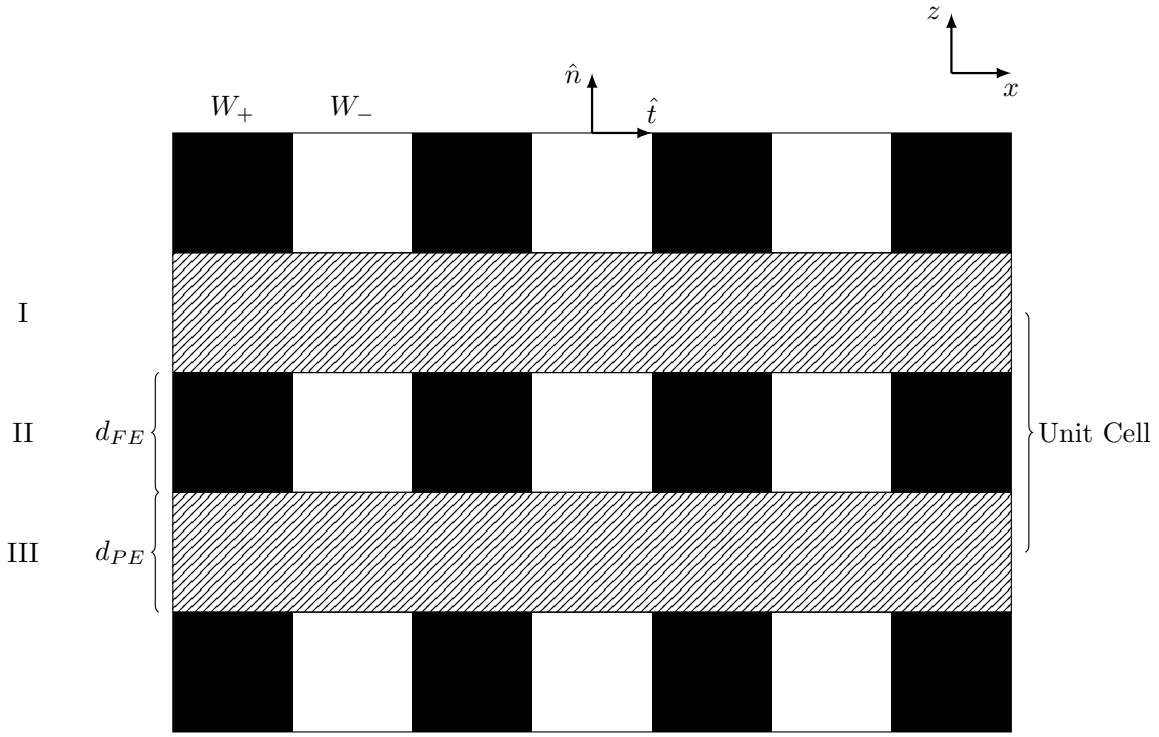

Fig. 2.4 A superlattice of alternating ferroelectric and paraelectric layers. Region II corresponds to the ferroelectric layer and regions I and III each correspond to half of the paraelectric layer.

Next, we describe the electrostatics of a superlattice consisting of alternating ferroelectric and paraelectric layers, shown in Figure 3.2. We solve for the electrostatics of a single unit cell and impose periodic boundary conditions, obtaining expressions for the total energy per unit cell. In the interest of symmetry, we will center the system in the middle of a ferroelectric layer and a positive domain.

As with the previous cases, we use a Fourier series representation of the polarisation, treating the $n = 0$ and the $n \neq 0$ terms separately. The $n = 0$ terms will be the same as the monodomain case with spontaneous polarisation AP_S. However as we are dealing with a periodic superlattice, the electrostatics for the monodomain case will not be the same as before; there will be electric field inside the paraelectric layers. Assuming there is a constant field in both of the layers, the potential will have a zig-zag-type form as shown in Figure 2.5.

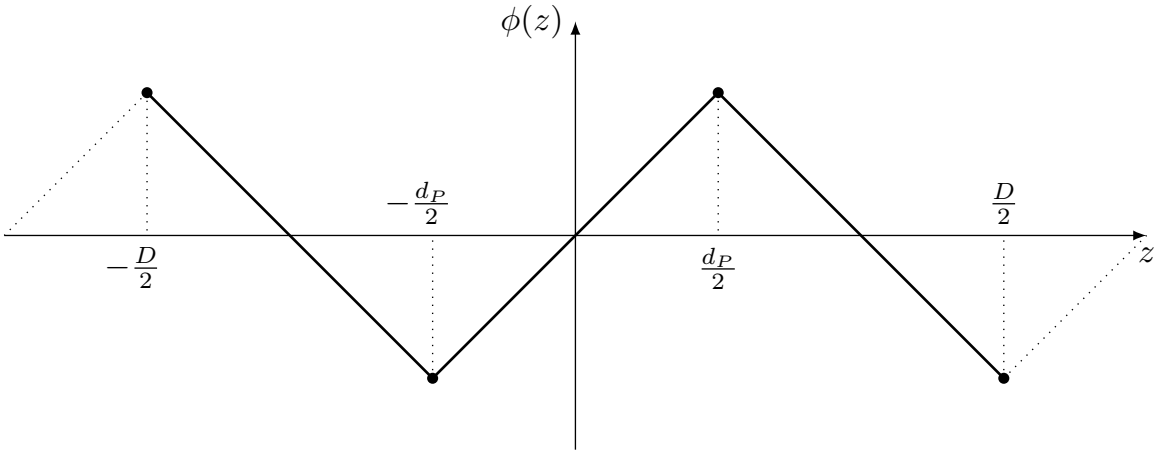

Fig. 2.5 The electrostatic potential inside the superlattice in the monodomain case.

After applying the correct boundary conditions, we find that the potentials are of the form

$$\begin{aligned}
\phi_{\mathrm{I}}(z) &= -\frac{AP_S}{\varepsilon_0\left[\frac{\kappa_c}{d_{\mathrm{FE}}}+\frac{\kappa_s}{d_{\mathrm{PE}}}\right]d_{\mathrm{PE}}}(z-D/2) \\
\phi_{\mathrm{II}}(z) &= \frac{AP_S}{\varepsilon_0\left[\frac{\kappa_c}{d_{\mathrm{FE}}}+\frac{\kappa_s}{d_{\mathrm{PE}}}\right]d_{\mathrm{FE}}}z \\
\phi_{\mathrm{III}}(z) &= -\frac{AP_S}{\varepsilon_0\left[\frac{\kappa_c}{d_{\mathrm{FE}}}+\frac{\kappa_s}{d_{\mathrm{PE}}}\right]d_{\mathrm{PE}}}(z+D/2)
\end{aligned} \quad , \tag{2.62}$$

where $D = d_{\mathrm{FE}} + d_{\mathrm{PE}}$ is the length of the unit cell. For a thin film on a substrate, we checked that the vacuum case was reproduced by taking the limit $\kappa_s \to 1$. We can do the same here by letting $d_{\mathrm{PE}} \to \infty$ and $\kappa_s \to 1$. When we do this, we see that the fields in the paraelectric layers vanish, and the field in the ferroelectric layer is the same as the one in a thin film; a good sanity check. The electric field in the paraelectric half-layers is

$$E_{\mathrm{I,III}} = -\partial_z \phi_{\mathrm{I/III}} = \frac{AP_S}{\varepsilon_0\left[\frac{\kappa_c}{d_{\mathrm{FE}}}+\frac{\kappa_s}{d_{\mathrm{PE}}}\right]} , \tag{2.63}$$

and the energy in regions I and III is given by

$$U_{\mathrm{I+III}} = \frac{A^2P_S^2}{2\varepsilon_0\left[\frac{\kappa_c}{d_{\mathrm{FE}}}+\frac{\kappa_s}{d_{\mathrm{PE}}}\right]^2}\frac{\kappa_s}{d_{\mathrm{PE}}} . \tag{2.64}$$

Similarly, the energy in the ferroelectric layer is given by

$$U_{\mathrm{II}} = \frac{A^2 P_S^2}{2\varepsilon_0 \left[\frac{\kappa_c}{d_{\mathrm{FE}}} + \frac{\kappa_s}{d_{\mathrm{PE}}}\right]^2} \frac{\kappa_c}{d_{\mathrm{FE}}} \,. \tag{2.65}$$

Adding these together, they simplify nicely and we find that

$$U_{\mathrm{mono}} = \frac{A^2 P_S^2}{2\varepsilon_0 \left[\frac{\kappa_c}{d_{\mathrm{FE}}} + \frac{\kappa_s}{d_{\mathrm{PE}}}\right]} \,, \tag{2.66}$$

which resembles the case of the thin film. The factor inside the square brackets resembles an effective permittivity for the superlattice. We have to be cautious however, as this expression is not per unit volume. If we take the limit $d_{\mathrm{PE}} \to \infty$ and then divide by d_{FE}, we obtain the thin film monodomain energy.

Now for the $n \neq 0$ terms. Instead of imposing boundary conditions at $\pm\infty$, we impose periodic boundary conditions on the unit cell:

$$\begin{aligned}
\phi_{\mathrm{I}}(x,z) &= \sum_{n=1}^{\infty} \cos(nkx) \left(c_n^1 e^{nkz} + d_n^1 e^{-nkz}\right) \\
\phi_{\mathrm{II}}(x,z) &= \sum_{n=1}^{\infty} \cos(nkx) \left(c_n^2 e^{cnkz} + d_n^2 e^{-cnkz}\right) \,, \\
\phi_{\mathrm{III}}(x,z) &= \sum_{n=1}^{\infty} \cos(nkx) \left(c_n^3 e^{nkz} + d_n^3 e^{-nkz}\right)
\end{aligned} \tag{2.67}$$

where $k = \frac{2\pi}{W}$. Again, we have six coefficients to determine and therefore require six conditions. These are

$$\begin{aligned}
\phi_{\mathrm{I}}(d_{\mathrm{FE}}/2) &= \phi_{\mathrm{II}}(d_{\mathrm{FE}}/2) \\
\phi_{\mathrm{III}}(-d_{\mathrm{FE}}/2) &= \phi_{\mathrm{II}}(-d_{\mathrm{FE}}/2) \\
\phi_{\mathrm{I}}(D/2) &= \phi_{\mathrm{III}}(-D/2) \\
(\vec{D}_{\mathrm{I}} - \vec{D}_{\mathrm{II}}) \cdot \hat{n} &= 0 \\
(\vec{D}_{\mathrm{III}} - \vec{D}_{\mathrm{II}}) \cdot \hat{n} &= 0 \\
\phi_{\mathrm{I}}(z) &= -\phi_{\mathrm{III}}(-z)
\end{aligned} \,. \tag{2.68}$$

The first two arise from matching the potentials at the interfaces. The third comes from imposing periodic boundary conditions on the unit cell. The fourth and fifth are the matching

of the displacement fields at the interfaces, and the last is due to the symmetry of the system under $z \to -z$. We use the symmetry condition to obtain

$$\begin{aligned} c_n^1 &= -d_n^3 \\ d_n^1 &= -c_n^3 \end{aligned} , \tag{2.69}$$

which simplifies things greatly. If we use the periodic boundary conditions, we get

$$d_n^1 = -c_n^1 e^{nkD} , \tag{2.70}$$

which gives

$$\begin{aligned} \phi_{\mathrm{I}}(x,z) &= \sum_{n=1}^{\infty} c_n^1 \cos(nkx) \sinh(nk(z-D/2)) \\ \phi_{\mathrm{II}}(x,z) &= \sum_{n=1}^{\infty} \cos(nkx) \left(c_n^2 e^{cnkz} + d_n^2 e^{-cnkz} \right) \\ \phi_{\mathrm{III}}(x,z) &= \sum_{n=1}^{\infty} c_n^1 \cos(nkx) \sinh(nk(z+D/2)) \end{aligned} . \tag{2.71}$$

Matching the displacement fields and the potentials at the interfaces, we quickly see that

$$\phi_{\mathrm{II}}(x,z) = \sum_{n=1}^{\infty} c_n^2 \cos(nkx) \sinh(cnkz) , \tag{2.72}$$

and

$$c_n^1 = -\frac{\sinh\left(cnk\frac{d_{\mathrm{FE}}}{2}\right)}{\sinh\left(nk\frac{d_{\mathrm{PE}}}{2}\right)} c_n^2 = -\beta_n c_n^2 , \tag{2.73}$$

where we define

$$\beta_n = \frac{\sinh\left(cnk\frac{d_{\mathrm{FE}}}{2}\right)}{\sinh\left(nk\frac{d_{\mathrm{PE}}}{2}\right)} . \tag{2.74}$$

Finally, matching the displacement fields at the boundary again gives

$$\left[\kappa_c \partial_z \phi_{\mathrm{II}} - \kappa_s \partial_z \phi_{\mathrm{I}}\right]_{d_{\mathrm{FE}}/2} = \frac{1}{\varepsilon_0} \frac{4P_S}{n\pi} \sin\left(\frac{n\pi}{2}(A+1)\right) \cos(nkx) , \tag{2.75}$$

which yields

$$c_n^2 = \frac{1}{\varepsilon_0}\frac{4P_S}{n^2\pi k}\gamma_n \sin\left(\frac{n\pi}{2}(A+1)\right), \tag{2.76}$$

where

$$\gamma_n = \left[g\cosh\left(cnk\frac{d_{\mathrm{FE}}}{2}\right) + \kappa_s \coth\left(nk\frac{d_{\mathrm{PE}}}{2}\right)\sinh\left(cnk\frac{d_{\mathrm{FE}}}{2}\right)\right]^{-1}. \tag{2.77}$$

Finally, the electrostatic potentials are given by

$$\begin{aligned}
\phi_{\mathrm{I}}(z) &= -\frac{AP_S}{\varepsilon_0\left[\frac{\kappa_c}{d_{\mathrm{FE}}}+\frac{\kappa_s}{d_{\mathrm{PE}}}\right]d_{\mathrm{PE}}}(z-D/2) - \sum_{n=1}^{\infty}\alpha_n\beta_n\gamma_n\cos(nkx)\sinh(nk(z-D/2)) \\
\phi_{\mathrm{II}}(z) &= \frac{AP_S}{\varepsilon_0\left[\frac{\kappa_c}{d_{\mathrm{FE}}}+\frac{\kappa_s}{d_{\mathrm{PE}}}\right]d_{\mathrm{FE}}}z + \sum_{n=1}^{\infty}\alpha_n\gamma_n\cos(nkx)\sinh(cnkz) \\
\phi_{\mathrm{III}}(z) &= -\frac{AP_S}{\varepsilon_0\left[\frac{\kappa_c}{d_{\mathrm{FE}}}+\frac{\kappa_s}{d_{\mathrm{PE}}}\right]d_{\mathrm{PE}}}(z+D/2) - \sum_{n=1}^{\infty}\alpha_n\beta_n\gamma_n\cos(nkx)\sinh(nk(z+D/2))
\end{aligned}, \tag{2.78}$$

where

$$\alpha_n = \frac{4P_S}{\varepsilon_0 n^2\pi k}\sin\left(\frac{n\pi}{2}(A+1)\right). \tag{2.79}$$

These expressions reduce to the monodomain expressions when $A \to 1$, as only the $n = 0$ terms survive. We should check the $d_{\mathrm{PE}} \to \infty$ limit to make sure they reduce to the case of a thin film. The vacuum thin film expression is obtained when $d_{\mathrm{PE}} \to \infty$ and $\kappa_s \to 1$, which is reassuring.

It remains to calculate the energy for the $n \neq 0$ terms. First, we consider regions I and III. Using the orthogonality relations as before, the integrals in the x-direction both evaluate to $\frac{1}{2}\delta_{nm}$ and the energy *per unit area* is given by

$$U_{\mathrm{I+III}} = \frac{1}{4}\varepsilon_0\kappa_s\sum_{n=1}^{\infty}(nk)\alpha_n^2\beta_n^2\gamma_n^2\sinh(nkd_{\mathrm{PE}}). \tag{2.80}$$

Similarly, the energy in region II is given by

$$U_{\mathrm{II}} = \frac{1}{4}\varepsilon_0 g\sum_{n=1}^{\infty}(nk)\alpha_n^2\gamma_n^2\sinh(cnkd_{\mathrm{FE}}). \tag{2.81}$$

Therefore, the total energy of the unit cell is

$$U_{\text{dep}} = \frac{A^2 P_S^2}{2\varepsilon_0 \left[\frac{\kappa_c}{d_{\text{FE}}} + \frac{\kappa_s}{d_{\text{PE}}}\right]} + \\ + \frac{1}{4}\varepsilon_0 \sum_{n=1}^{\infty} (nk)\alpha_n^2 \gamma_n^2 \left[g \sinh\left(cnkd_{\text{FE}}\right) + \beta_n^2 \kappa_s \sinh\left(nkd_{\text{PE}}\right)\right] \quad . \tag{2.82}$$

This also reduces to the vacuum case when $d_{\text{PE}} \to \infty$, $\kappa_s \to 1$. After a bit of algebra, each term in the series simplifies considerably

$$U_{n\neq 0} = \frac{8P_S^2}{\varepsilon_0 \pi^3} w \sum_{n=1}^{\infty} \frac{\sin^2\left(\frac{n\pi}{2}(A+1)\right)}{n^3} \frac{1}{g \coth\left(\frac{cn\pi}{2}\frac{d_{\text{FE}}}{w}\right) + \kappa_s \coth\left(\frac{n\pi}{2}\frac{d_{\text{PE}}}{w}\right)} \, , \tag{2.83}$$

which looks relatively tidy and resembles the expression for the energy of a thin film. As discussed previously, this expression has the expected behaviour in the monodomain limit. At this point it is important to consider the units of this energy. The normalisation of each energy term in the Landau theory requires careful consideration, as some terms are only associated with the ferroelectric layer and others are associated with the entire unit cell. Previously, the energies were given per unit volume of the thin film. As the depolarising energy is associated with the entire unit cell, we divide by D and express it per unit cell volume. Since later it will become useful to work in terms of the thickness of the ferroelectric layer, we let

$$\begin{aligned} d &= d_{\text{FE}} \\ \alpha &= \frac{d_{\text{PE}}}{d_{\text{FE}}} \end{aligned} \, , \tag{2.84}$$

so that

$$\begin{aligned} d_{\text{PE}} &= \alpha d \\ D &= (1+\alpha)d \end{aligned} \, . \tag{2.85}$$

Dividing by $D = (1+\alpha)d$ and taking the limit $r = d/w \gg 1$ as before, we obtain a Kittel expression,

$$U_{\text{Kittel}} = \frac{P_S^2}{2\varepsilon_0} \beta(\kappa_s, \alpha) \frac{1}{r} \, , \tag{2.86}$$

with

$$\beta(\kappa_s, \alpha) \approx \frac{16.829\ldots}{\pi^3(1+\alpha)(g+\kappa_s)} \,. \tag{2.87}$$

The constant $\beta(\kappa_s, \alpha)$ not only depends on the permittivity of the paraelectric layer but also on α, the ratio of thicknesses of the layers. In the limits $\kappa_s \to 1$ and $\alpha \to 0$ ($d_{\mathrm{PE}} \to \infty$), it reduces to the β that appears in the standard Kittel law.

2.2 Landau Theory

Having obtained the electrostatic descriptions, we proceed to analyse the behaviour of the screening mechanisms using a Landau theory.

2.2.1 Kittel Law

First, we can use a Landau theory to derive the Kittel law for each of the systems. In the context of ferroelectrics, this is often referred to the Kittel-Mistui-Furuichi (KMF) law, as the original Kittel law was derived for ferromagnetic materials. We start with the energy *per unit volume* of a ferroelectric material in the polydomain limit,

$$U_{\mathrm{KMF}} = U_0(P_S) + \frac{\Sigma}{w} + \frac{P_S^2}{2\varepsilon_0}\beta(\kappa_s, \alpha)\frac{w}{d} \,, \tag{2.88}$$

where U_0 is the double-well-type energy associated with the polarisation and Σ is the energy cost of creating a ferroelectric domain wall. We assume that the polarisation is fixed at P_S, so the material is in a stable ferroelectric state. This theory is used to derive the Kittel law for a thin film in a vacuum, but we can extend it to thin films on substrates and superlattices using the expressions for β derived in the previous section. It is important to note here that in the superlattice, there may be a weaker domain structure induced in the paraelectric layers. This effect may prove important and should be introduced to the free energy. There are a number of possible ways to treat this. We could assume that it contributes the same energy as the domains in the ferroelectric layer, but this would be an exaggeration. We could use first-principles calculations to determine the energy cost, Σ_{PE}, associated with the induced domain walls, which would be the most thorough option. For now, we assume that its energetic contribution is much weaker than the domain walls in the ferroelectric layers and neglect it.

For the superlattice, the other terms in the free energy must be re-normalised appropriately. As the polarisation and domain wall energies are associated with the ferroelectric layer, we normalise them by

$$\frac{d_{\mathrm{FE}}}{d_{\mathrm{FE}}+d_{\mathrm{PE}}}=\frac{1}{1+\alpha}\,. \tag{2.89}$$

Each term in the free energy is normalised by a factor of $(1+\alpha)^{-1}$, indicating that the ratio of thicknesses in the superlattice scales the overall free energy, but has no effect on the behaviour of the screening mechanisms. This is not surprising as we are working in the polydomain limit; the monodomain limit has a more intrinsic dependence on α. We minimise the free energy with respect to the domain widths, leading to the Kittel or KMF law:

$$w=\sqrt{l_k d}\,, \tag{2.90}$$

where

$$l_k(\kappa_s)=\frac{2\varepsilon_0\Sigma}{P_S^2\beta(\kappa_s)}\,. \tag{2.91}$$

$l_k(\kappa_s)$ is the Kittel length, which defines the relevant length scale of the systems. We note that the dependence on α has vanished in the case of the superlattice. This modified version of the Kittel law describes the dependence of the domain walls on the permittivities of the substrate and paraelectric layers. This is an important result, as the Kittel law originally only described materials in a vacuum. Figure 2.6 shows a plot of the Kittel law for three different cases: a thin film of PTO in a vacuum, a thin film of PTO on a substrate and a superlattice of PTO and a paraelectric material. The substrate and paraelectric layer in the superlattice have a permittivity of $\kappa_s=100$ to illustrate their influence on the domains. We can see from this plot that in the case of the substrate and the superlattice, the domains are larger than those in a thin film in a vacuum of the same thickness. This makes sense because the constant β decreases with increasing κ_s, implying that the depolarising energy decreases with the permittivity of the substrate and paraelectric layers in the superlattice. Balancing the energy in the Landau theory, this leads to a decrease in the domain energy, leading to fewer domain walls and hence larger domains. The walls in the superlattice are smaller than the ones in the thin film on a substrate, which is not surprising. Although the energies were taken per unit volume of thin film and superlattice unit cell, the electric field in the substrate was integrated over an infinite range, so it has a bigger contribution to the energy than the paraelectric layers.

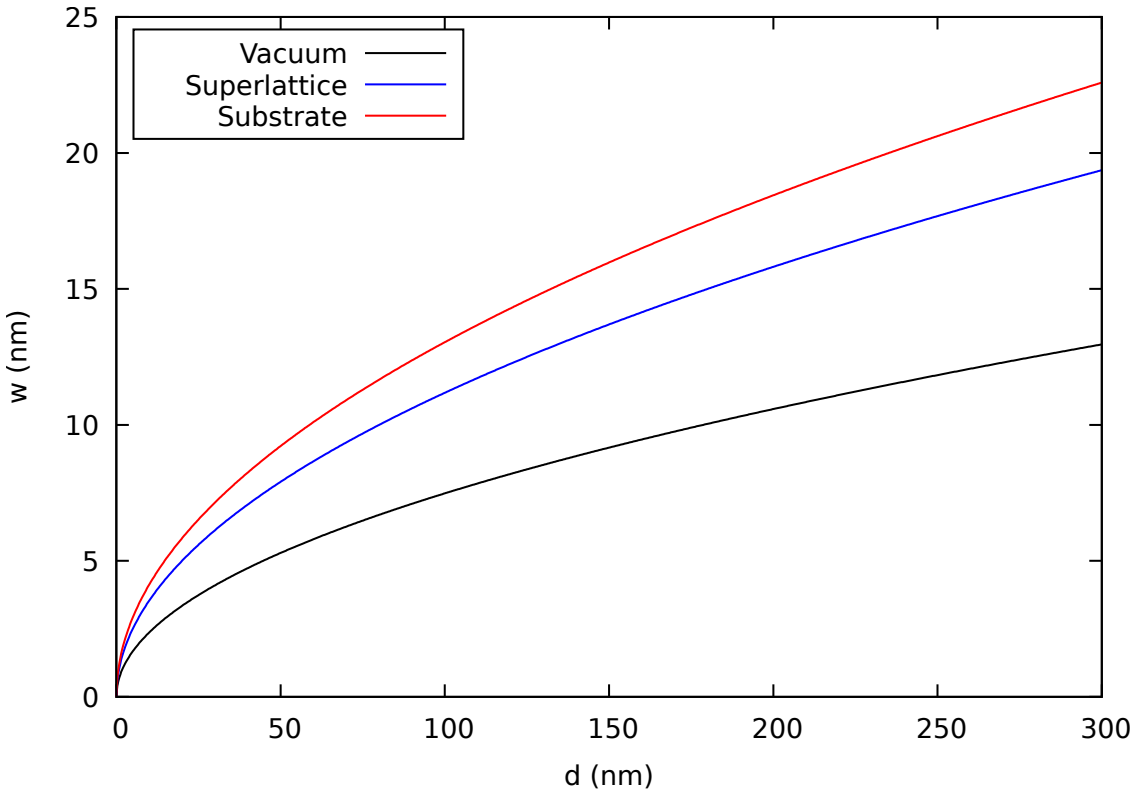

Fig. 2.6 The Kittel law for a thin film of PTO in a vacuum, a thin film of PTO on a substrate of permittivity $\kappa_s = 100$, and a superlattice of alternating layers of PTO and the same material.

2.2.2 Coexistence Model

Next, we use a Landau theory to model coexistence between ferroelectric domains and a 2DEG at the surfaces and interfaces of ferroelectric materials. The free energy for such a system is a combination of the free energies associated with the two screening mechanisms in isolation. Of course, we must modify the depolarising energy appropriately as it is common to both situations. In order to modify the electrostatics to account for the 2DEG, we must modify the boundary conditions in Maxwell's equations for the displacement fields,

$$(\vec{D}_{\mathrm{I}} - \vec{D}_{\mathrm{II}}) \cdot \hat{n} = \sigma \, . \tag{2.92}$$

This can be accounted for with

$$P \to P - \sigma \, . \tag{2.93}$$

Thus, the free energy is given by

$$U(P, w, \sigma) = U_0(P) + \frac{\Delta\sigma}{d} + \frac{\sigma^2}{2gd} + \frac{\Sigma}{w} + U_{\mathrm{dep}}(P - \sigma, w, d) \, . \tag{2.94}$$

This resembles (2.88), but the depolarising energy is screened by the 2DEG and there are two additional terms associated with the 2DEG. These additional terms account for the cost of promoting electrons from the conduction band to the valence band. The second term is the energy cost of charge transfer across the gap, Δ. This gap has different physical interpretations depending on the geometry of the system and the origin of the 2DEG [14]. In the case of a thin film in a vacuum, Δ is simply the band gap, however with a substrate or in a superlattice, the band offset at the interface should be taken into account. The third term is the cost of filling the bands, with finite density of states. Here, we use the reduced density of states,

$$g = \frac{g_e g_h}{g_e + g_h} \, , \tag{2.95}$$

where g_e and g_h are the density of states for electrons and holes, respectively. In the previous section we used the Kittel approximation for the depolarising energy, but in general it will be given by the complete electrostatic expressions derived in the previous section. The full electrostatic expressions are represented by infinite series and lead to equations which are quite volatile and can only be solved using numerical methods. Using the Kittel expressions will allow us to obtain analytic approximations, however. We derive the analytic solutions using the Kittel energies and compare to numerical solutions using the complete electrostatic

energies truncated after a large number of terms. As in the previous section, we fix the polarisation at the spontaneous polarisation, P_S. The free energy to be minimised is

$$U(w,\sigma) = U_0(P_S) + \frac{\Delta\sigma}{d} + \frac{\sigma^2}{2gd} + \frac{\Sigma}{w} + \frac{(P_S-\sigma)^2}{2\varepsilon_0}\beta(\kappa_s,\alpha)\frac{w}{d}\,, \tag{2.96}$$

which is not specific to any of the three systems. Once again, we must be careful in how we normalise the energy of the superlattice. Each term is scaled by a factor of $(1+\alpha)^{-1}$, meaning the overall scaling of the energy, but not the actual behaviour of the screening mechanisms, is affected by α. We minimise with respect to the domain width, and surface charge, in order to determine how they depend on the thickness:

$$\partial_w G = \partial_\sigma G = 0\,. \tag{2.97}$$

This leads to a pair of coupled nonlinear equations,

$$\begin{aligned} -\frac{\Sigma}{w^2} + \frac{(P_S-\sigma)^2}{2\varepsilon_0}\beta(\kappa_s)\frac{1}{d} &= 0 \\ \frac{\Delta}{d} + \frac{\sigma}{gd} - \frac{(P_S-\sigma)}{\varepsilon_0}\beta(\kappa_s)\frac{w}{d} &= 0 \end{aligned}\,. \tag{2.98}$$

Using the first equation, we can isolate w,

$$w = \frac{1}{(P_S-\sigma)}\sqrt{\frac{2\varepsilon_0\Sigma}{\beta(\kappa_s)d}}\,, \tag{2.99}$$

and then replacing it in the second equation, we get

$$\begin{aligned} \frac{\Delta}{d} + \frac{\sigma}{gd} - \sqrt{\frac{2\Sigma\beta(\kappa_s)}{\varepsilon_0 d}} &= 0 \\ \implies \sigma(d) = g\Delta\left(\sqrt{\frac{2\Sigma\beta(\kappa_s)d}{\varepsilon_0\Delta^2}} - 1\right) & \end{aligned}\,. \tag{2.100}$$

Since we require σ to be non-negative, we find that there is a critical thickness, d_c, below which there is no surface charge,

$$d_c = \frac{\varepsilon_0\Delta^2}{2\Sigma\beta(\kappa_s)}\,, \tag{2.101}$$

and thus the surface charge is given by

$$\sigma(d) = g\Delta\left(\sqrt{\frac{d}{d_c}} - 1\right), \tag{2.102}$$

We can use this to find the thickness, d_p, at which the surface charge saturates, i.e. $\sigma(d_p) = P_S$,

$$d_p = d_c\left(1 + \frac{P_S}{g\Delta}\right)^2. \tag{2.103}$$

This is also the thickness at which the width of the domains diverges. Returning to the equations, we now solve for w,

$$w(d) = \frac{\sqrt{l_k d}}{\left[1 - \frac{g\Delta}{P_S}(\sqrt{\frac{d}{d_c}} - 1)\right]}, \tag{2.104}$$

where l_k is the Kittel length. Equations (2.102) and (2.104) are the analytic result of the coexistence model in the Kittel limit. These results are valid for a thin film in a vacuum, a thin film on a substrate and a superlattice, and each case can be analysed with the correct choice of $\beta(\kappa_s)$. Figure 2.7 shows a plot of (2.102) and (2.104) for a thin film of PTO in a vacuum and on a substrate of permittivity $\kappa_s = 10$ as well as numerical solutions using the full electrostatic expressions, truncated at 1000 terms. What is important to note here is that the range in which coexistence can be sustained has been shifted to the right but also extended due to the permittivity of the substrate. For the vacuum case, the range of coexistence, $|d_p - d_c|$, is approximately 206.9 nm and for the substrate case, the range has increased to approximately 241.9 nm. Similar results were obtained for the superlattice. It was found that, for both the numerical and analytic solutions, there was little or no dependence on α, the ratio of thicknesses of the layers.

In summary, we have extended the model of coexistence to describe a thin film in a vacuum or on a substrate, as well as superlattices. It was found that the substrate and the paraelectric layers in the superlattice extend the range where coexistence between domains and a 2DEG can be achieved. This is important, since, as mentioned previously, the permittivity of STO can be very large, possibly leading to a very wide coexistence range for a thin film of PTO grown on a substrate of STO, or in PTO/STO superlattices.

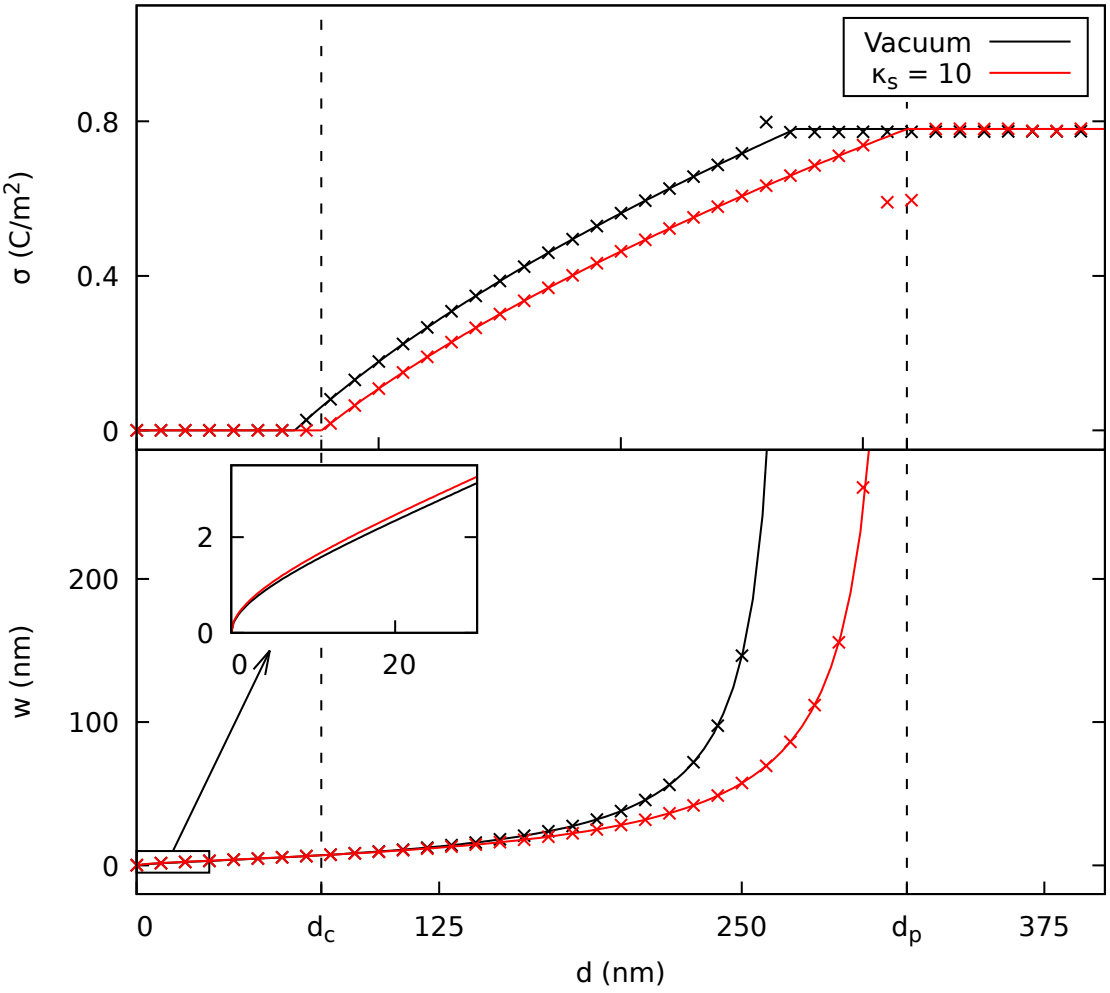

Fig. 2.7 Analytic and numerical results of the coexistence model for a thin film in a vacuum and a thin film on a substrate of permittivity $\kappa_s = 10$. The numerical results used the full electrostatic depolarising energy, truncating the series after 1000 terms. The deviations of σ from the analytic result around and above d_p are due to the volatile nature of the equations when using the full electrostatics. It is important to note that in the inset, there is a slight difference between the coexistence model and the Kittel behaviour. This is because below d_c, the analytic expression for σ is negative, which is unphysical. We set σ to be zero below d_c, but the analytic expression for w was obtained before imposing this condition.

Chapter 3

First-Principles Calculations

With the increase in computing power in recent decades, first-principles electronic structure methods such as density functional theory (DFT) have become extremely popular and useful in physics, chemistry and materials science [20]. DFT calculations are a quick and cheap way of studying the structural, electronic and other properties of physical systems and materials. While DFT calculations are certainly not a replacement for physical experiments, they can serve as a useful indicator as to how a particular system might behave. As there is an abundance of excellent resources on the theory behind DFT in the literature, it is not necessary to review it here. Relevant details of the computational methods will be described in the following section and Appendix A, however.

In this chapter we describe the first-principles simulations performed to study screening mechanisms in ferroelectric materials. As mentioned in the introduction, we use thin films of PTO in a vacuum and PTO/STO superlattices as test cases, introducing the 2DEG to our simulations through atomic defects.

In order to study the screening mechanisms considered in the previous chapter computationally, very large supercells, consisting of hundreds of atoms would be required. For example, to simulate ferroelectric domains, a supercell generated by repeating the primitive cell a large number of times in a direction(s) normal to the surface would be required. Assuming the domain widths to be equal, half of the cells would be polarised in one direction and the other half in the opposite direction. In order to screen the depolarising field with a 2DEG, a surface charge close to the spontaneous polarisation is required. For example, using the values of $P_S = 0.78$ C/m^2 and $a = 3.86$ Å for bulk PTO obtained from first-principles calculations, we would need a surface charge of

$$\sigma = 0.78 \text{ C/m}^2 \approx 0.73 \frac{\text{e}}{\Omega} , \tag{3.1}$$

i.e. 0.73 electrons per unit cell surface area, to screen the depolarising field. Introducing a fractional vacancy per primitive cell typically requires the use of large supercells, meaning as with the domains, a 2DEG would be expensive to simulate. While supercell calculations are lengthy and more computationally demanding, they are necessary in order to study the screening mechanisms. Since the polarisation is related to the displacements of the atoms in the unit cell, a time-consuming geometry relaxation is required for each calculation.

In order to avoid calculations which could take days, or even weeks, we make use of a method which will allow us to introduce a fractional concentration of defects to a single unit cell. This will allow us to study the effect of 2DEGs on monodomain thin films and superlattices without the use of large supercells[1]. The geometries obtained from these calculations can be used as reference configurations in larger supercell calculations with defects and domains in the future, potentially saving a great deal of computational expense.

3.1 Virtual Crystal Approximation

The virtual crystal approximation (VCA) was historically used in first-principles calculations to study disordered alloys and solid solutions without the use of large supercells [21]. The VCA uses a primitive unit cell composed of 'virtual' atoms which interpolate between their composite components. This method reduces the computational effort required greatly, but the accuracy of the VCA applied to various systems has shown mixed results. While many studies have reported success in using the VCA to study some ferromagnetic and semiconducting materials [22, 23], others have shown that the method is inadequate for the description of the electronic structure of certain semiconducting systems [24]. The VCA was considered an unreliable method as its accuracy appeared to be dependent on the system in question. Fortunately, it has been shown that the VCA can be used to describe ferroelectric perovskite solid solutions accurately [25].

The VCA creates a virtual atom by mixing the pseudopotentials of the two parent atoms. For example, consider the mixing of two parent atoms, A and B, both of which are described by

[1] Obviously to simulate thin films and supercells, the bulk primitive cell is repeated a number of times in the z-direction. Here the supercells we are referring to are ones that are also repeated several times in the x- and/or y-directions.

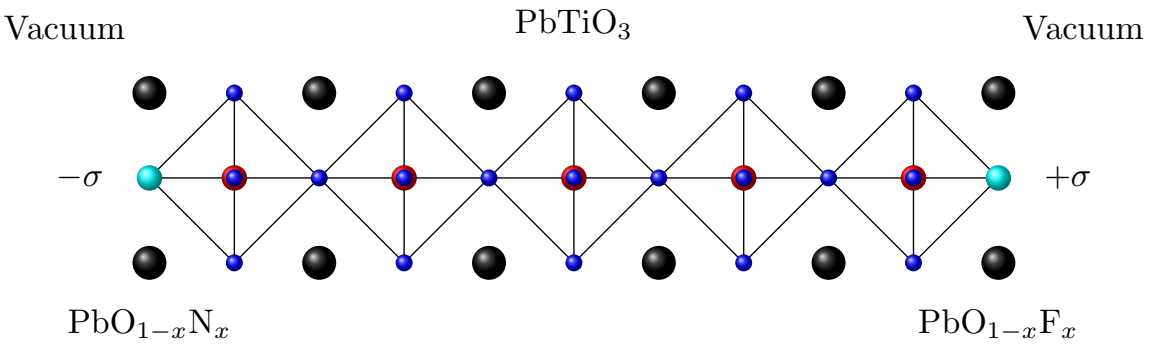

Fig. 3.1 A thin film of PTO with virtual atoms (cyan) at the surfaces. The oxygen atom on the left is replaced with the virtual atom $O_{1-x}N_x$, creating a surface charge of x electrons per unit cell. The oxygen atom on the right is replaced with the virtual atom $O_{1-x}F_x$, creating a surface charge of $-x$ electrons per unit cell.

local pseudopotentials. The virtual atom, A_xB_{1-x}, where x is the mixing fraction, is described by a mixed pseudopotential:

$$V_{\mathrm{VCA}}(\mathbf{r}) = xV_A(\mathbf{r}) + (1-x)V_B(\mathbf{r}) \; . \tag{3.2}$$

While the VCA was typically used to model alloys and disordered systems, here we use it to introduce the 2DEGs, controlling the surface charges and hence the displacement fields in thin films. A virtual atom is created and placed at the surface by mixing one of the atoms at the surface with a neighbouring atom in the periodic table. The resultant virtual atom results in a surface charge at the interface. We can use a dipole correction to remove the displacement field in the vacuum region, which arises due to spurious interactions between the system and its periodic images [26]. Having removed the field in the vacuum region, we can directly relate the displacement field in the thin film to the surface charges. Therefore, since the surface charges are specified by the VCA, we can control the displacement field in the thin films.

In the context of perovskite thin films, we can introduce a 2DEG through oxygen defects. Consider a PbO-terminated thin film of PTO. In order to create a surface charge, we replace the oxygen atoms at the surfaces or interfaces with virtual atoms of oxygen mixed with nitrogen and fluoride (see Figure 3.1). This generates surface charges of magnitude $\sigma = x$ electrons per unit cell surface area. If we were to perform simulations with real defects, we would have oxygen vacancies on one surface and lead vacancies on the other. However in the interest of symmetry, we use oxygen defects on both surfaces of the thin film. The

displacement field in the vacuum region is removed using a dipole correction, and the field inside the film becomes

$$\vec{D} = -x \frac{\mathrm{e}}{\Omega}, \tag{3.3}$$

where Ω is the surface area normal to the interfaces. We cannot directly control the displacement fields in periodic superlattices as there is also a field in the paraelectric layers, but we can still use the VCA to introduce 2DEGs at the interfaces.

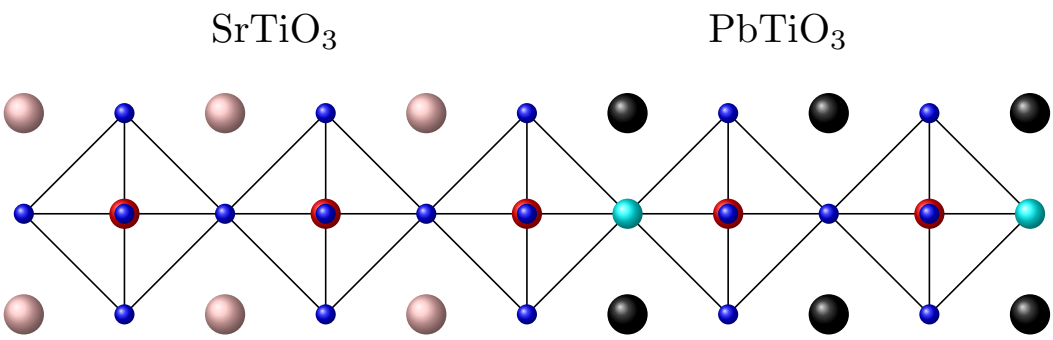

Fig. 3.2 The unit cell of a periodic superlattice, comprised of a layer of ferroelectric PTO and a layer of paraelectric STO. The virtual atoms are introduced at the interfaces between the layers.

3.2 Computational Methods

Here we describe the computational methods for the simulation and characterisation of the thin films and superlattices. DFT calculations were performed using the SIESTA method and program, which employs numerical atomic orbitals [27]. All calculations were performed within the local density approximation (LDA) using the Ceperley-Alder exchange-correlation functional [28]. Norm-conserving Troullier-Martin pseudopotentials were used to replace the core electrons [29]. A Fermi-Dirac distribution with a temperature of 0.075 eV was used to smear the occupancy of the one-particle electronic states. Reciprocal space integrations were performed on a Monkhorst-Pack k-point mesh [30].

Pseudopotentials were generated using the ATOM program [31]. Due to the overlap between the semicore and valence states, the $5d$ electrons of Pb were explicitly included with the valence electrons. A scalar relativistic pseudopotential was generated using the reference configuration $6s^2$, $6p^2$, $5d^{10}, 5f^0$. Full details of the pseudopotentials are included in Ap-

pendix A.

Bulk PTO was initially considered for two reasons. Firstly, since there are only five atoms in the unit cell, it is easy to quickly test and converge our approximations and simulation parameters. Secondly, it provides a useful reference for the larger calculations; the bulk in-plane lattice constant is used to generate the thin films and superlattices. The distortions of the atoms and the polarisation of the bulk system will also serve as a useful reference when analysing the thin films and superlattices. As in the previous chapter, we take spontaneous polarisation of bulk PTO to be $P_s = 0.78$ C/m^2, obtained from [14] using the Born effective charge method [32]; a good approximation to the exact value given by the Berry phase formalism.

Using the theoretical lattice constant of 4 Å, bulk PTO in its cubic phase was used to test the convergence of the total energy with respect to the k-point mesh and the cutoff energy. It was found that a $6 \times 6 \times 6$ k-point mesh was sufficient to converge the total energy. A grid of $6 \times 6 \times 1$ was used for the thin films and superlattices. A cutoff energy of 600 Ry was enough to converge the total energy in the bulk system, however a cutoff energy of 300 Ry was used in order to keep the computational costs to a minimum.

After determining the appropriate convergence parameters, the geometry of the bulk system was analysed. Starting with the theoretical lattice constant of 4 Å, a relaxation of the atomic positions and the unit cell was performed using the conjugate gradient method in SIESTA. The atoms were slightly offset from their respective layers to prevent the system from remaining in the stable cubic phase. The system was then relaxed until the forces on all of the atoms were less than 0.01 eV/Å.

After successfully characterising the bulk system, a series of calculations were performed on thin films of PTO comprised of 4-8 layers. Thin films were generated by repeating the bulk unit cell a number of times in the z-direction. The thin film was separated from its periodic images using a vacuum of about 50 Å, and a dipole correction was introduced in this vacuum region to prevent interactions between the images. A 2DEG was introduced using the VCA by replacing the oxygen atoms on the surfaces with virtual atoms. A series of DFT calculations were performed for thin films ranging from 4-8 layers in thickness with surface charges ranging from 0-1 electrons per unit cell surface area. The films were relaxed in the presence of these surface charges. Geometry relaxations can be computationally expensive, so every effort was made to keep computation time to a minimum. Since increasing σ

sustains the polarisation and hence increases the distortion of the layers, calculations were performed in order, starting from the lowest value of σ. The relaxed geometry of the films without any surface charge was used as a starting point, and the relaxed geometry from this calculation was used as a starting point for the next calculation, and so on. This helped to reduce the number of geometry relaxation steps required.

Calculations of superlattices of ferroelectric PTO and paraelectric STO were then performed. A single unit cell in the *x*- and *y*-directions was used, and multiple layers of PTO and STO were used in the *z*-direction in order to create a periodically repeating superlattice. Calculations were performed using 3-6 layers each of PTO and STO. As PTO and STO have different lattice constants, there is an energy cost associated with the misfit strain introduced when forming a commensurate structure. This misfit strain was not studied here; starting from the theoretical lattice constant, a full variable cell geometry relaxation was performed in order to relax the geometries and find the lattice constant at which they form a commensurate structure. The VCA was then used to introduce the surface charge at the interfaces, and relaxations were then performed for a series of values of σ, using the aforementioned procedure to reduce the computational effort.

There are several different quantities we wish to examine from the output of the calculations. Since the methods of calculating the polarisation require the materials to be insulating, it is important to check that we have not changed the electronic structure of our systems by introducing virtual atoms. We can do this by examining the projected density of states (PDOS) of the different layers, in particular the layers containing virtual atoms, and verifying that the Fermi level is still contained in the gap.

After ensuring that our systems are still insulating, we need to calculate the polarisation to observe the screening effect of the 2DEG. This can be done using two different methods: by calculating the 'layer-by-layer polarisation' using the Born effective charges [32], and through the distortion of the layers. In the first method, the polarisation of each layer is calculated by adding the displacements of each atom with respect to the cation in that layer times the respective Born effective charge. The polarisation of each layer is then averaged over neighbouring layers such that each individual layer satisfies the acoustic sum rule. In the second method, the distortion of each layer is calculated:

$$\begin{aligned}\delta_z(\mathrm{PbO}) &= \delta_z(\mathrm{Pb}) - \delta_z(\mathrm{O_I}) \\ \delta_z(\mathrm{TiO_2}) &= \delta_z(\mathrm{Ti}) - \frac{(\delta_z(\mathrm{O_{II}}) + \delta_z(\mathrm{O_{III}}))}{2} \cdot\end{aligned} \tag{3.4}$$

We can infer the effective polarisation associated with these distortions by scaling with respect to the bulk configuration:

$$P_{\mathrm{eff}} = \frac{P_S}{\delta_{\mathrm{Bulk}}}\delta \,, \tag{3.5}$$

where $\delta_{\mathrm{Bulk}}(\mathrm{PbO})$ and $\delta_{\mathrm{Bulk}}(\mathrm{TiO_2})$ are the distortion of the layers in bulk PTO. It is important to note that surface effects will cause the outer layers of the films and superlattices to behave differently to the inner layers. Thus, when calculating polarisations using both methods, we neglect the outermost layers and average over the inner layers. It is also important to check that the depolarising field has been screened by the 2DEG. We can measure the electric fields by calculating the electrostatic potentials. The electrostatic potential can be obtained with the macroscopic averaging technique using the MACROAVE program within SIESTA [33, 34]. The planar averaged potential is first calculated in the z-direction,

$$\bar{V}(z) = \frac{1}{\Omega}\int_S V(\vec{r})\,\mathrm{d}x\,\mathrm{d}y \,. \tag{3.6}$$

A convolution is then performed to smooth out the oscillations of the potential. A step function is used,

$$\omega_l(z) = \frac{1}{l}\Theta\left(\frac{l}{2} - |z|\right) \,, \tag{3.7}$$

where l is approximately the thickness of the material. The smoothed potential is then given by

$$\bar{\bar{V}}(z) = \int \omega_l\left(z - z'\right)\omega_l\left(z - z''\right)\bar{V}\left(z''\right)\mathrm{d}z'\,\mathrm{d}z'' \,. \tag{3.8}$$

The slope of the smoothed potential inside the film gives an internal electric field, which is comparable to the drop in potential due to the dipole correction introduced in the vacuum region.

3.3 Results

Calculations for bulk PTO were performed to test convergence parameters. Values of $\delta_{\text{Bulk}}(\text{PbO}) = 0.356$ Å and $\delta_{\text{Bulk}}(\text{TiO}_2) = 0.297$ Å were obtained for the distortions of the layers, which were used to analyse the distortion of the layers in the thin films.

The VCA was then used to introduce a 2DEG of surface charges ranging from $\sigma = 0$ e/Ω to $\sigma = 1.0$ e/Ω in increments of 0.1. Calculations were also performed at $\sigma = 0.75$ e/Ω, which is close to the spontaneous polarisation of PTO. This was done for thin films comprised of 4-8 layers (an extra PbO half-layer was introduced to make the displacement field symmetric) and superlattices of 3/3, 6/3 and 6/6 layers of PTO/STO, respectively[2]. Results were similar across the range of thicknesses, as all of the simulations were in the range of a few nm in thickness; the results presented are for thin films of 8 layers and a superlattice of 6/6 layers in thickness. Firstly, it is important that our materials are insulating, and that the VCA has not changed the electronic structure in that way.

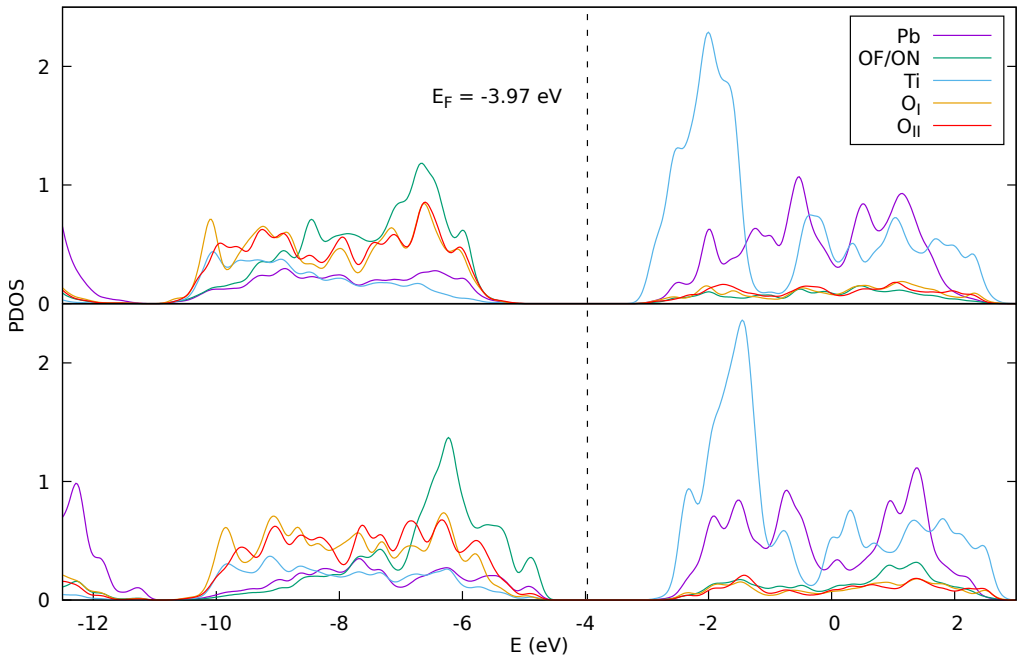

Fig. 3.3 The PDOS of the surface layers of a PTO thin film. The top plot is for the outer $PbO_{0.25}F_{0.75}$ and TiO_2 layers, and the bottom plot is for the outer $PbO_{0.25}N_{0.75}$ and TiO_2 layers. We can see that both layers remain insulating.

[2]Here, the number of layers corresponds to the number of bulk unit cells. When discussing the distortion, we refer to PbO/SrO and TiO_2 as separate layers.

The DOS and the PDOS were computed at each layer to check that our materials are still insulating. Figure 3.3 shows the PDOS at the surface layers of a thin film of PTO, where the VCA is introduced. We can also see that the superlattices are still insulating from the middle plot of Figure 3.8. This shows the PDOS for the TiO_2 layers; a similar plot of the PbO/SrO layers was obtained which confirmed that the superlattices are insulating.

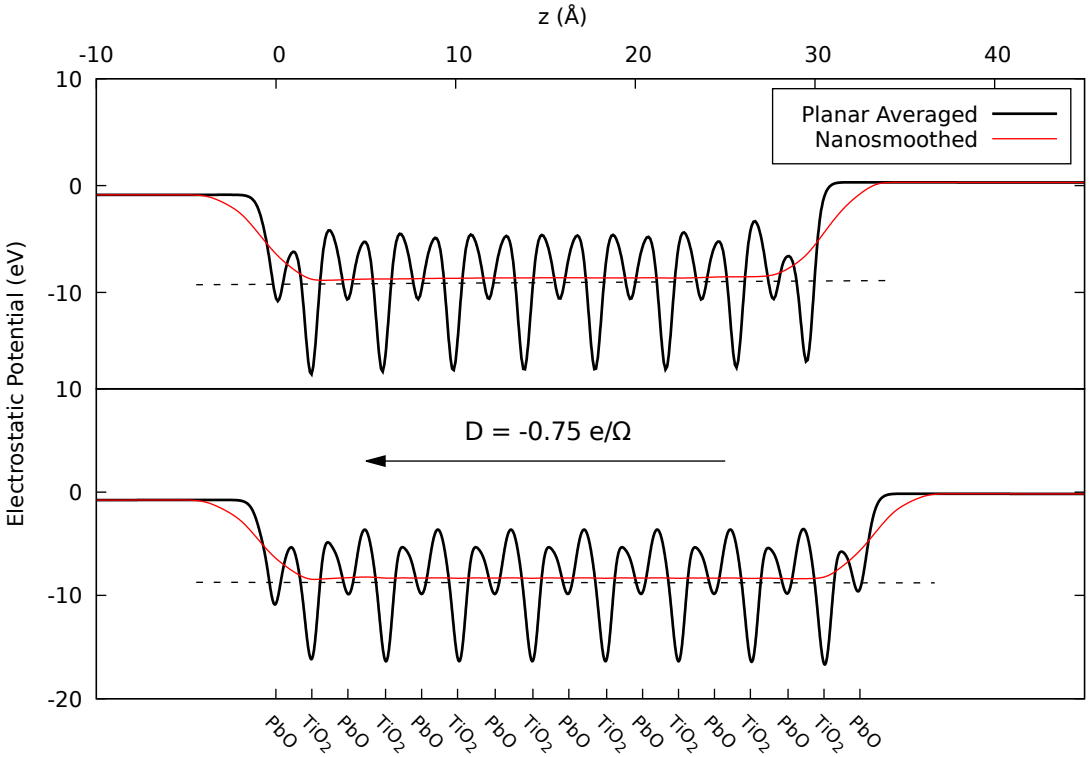

Fig. 3.4 The macroscopic potentials of PTO thin films with 2DEGs of $\sigma = 0$ e/Ω (top) and $\sigma = 0.75$ e/Ω (bottom). The dashed lines show a linear fit of the smoothed potentials inside the films, excluding the outer surface layers.

Having ensured that our materials are all insulating, the electrostatic potentials were obtained. Figure 3.4 shows the macroscopic planar averaged and nanosmoothed potentials inside thin films of PTO with $\sigma = 0$ e/Ω and $\sigma = 0.75$ e/Ω. These plots look very similar, noting in particular that the small slope of the potential inside the films, indicating that the depolarising field is very weak. While they are both very small, the reason for this is quite different in each case. In the first plot, this is due to the competition between the polarisation and the depolarising field. The depolarising field screens the polarisation, suppressing it, and as the polarisation decreases, a smaller depolarising field is required to screen it, and so on, leading to a situation where both the polarisation and depolarising field are very weak, but

nonzero. In the second plot, the slope represents the total electric field inside the thin film, which is comprised of not only the polarisation inside the film, but the dipole associated with the two surface charges introduced by the VCA. The surface charge and polarisation are of similar magnitude and opposite direction, so the total electric field inside the film is the difference between them, which is very small. For this reason, it is difficult to conclude that the depolarising field has actually been screened by σ in the second case, but we can confirm this and distinguish the two cases by calculating the polarisation of the materials.

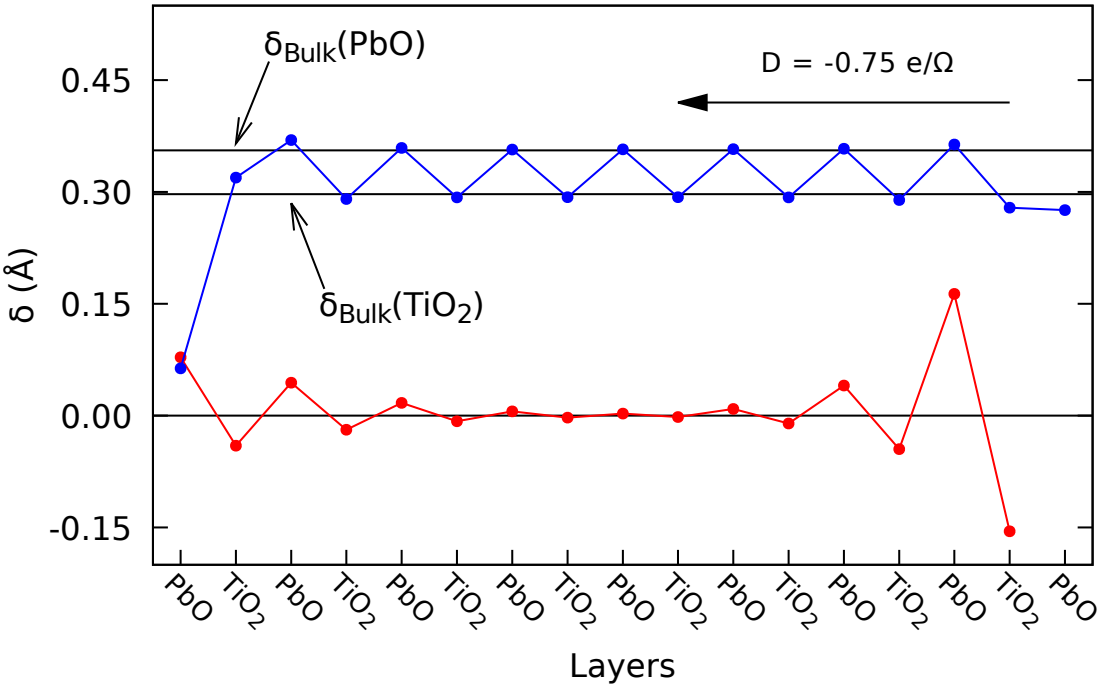

Fig. 3.5 The distortion of the layers for a thin film of PTO (blue) with a 2DEG of $\sigma = 0.75\ e/\Omega$, compared to the same film with no 2DEG (red). For the film with no 2DEG, an extra layer of PbO is not necessary. We see that when σ is close to the spontaneous polarisation, the distortion of the layers approaches those of the bulk.

The distortion of the individual layers were calculated using (3.4) and are shown in Figure 3.5. We can see that in the case of zero surface charge, there is barely any splitting of the layers, excluding surface effects, and hence a very small polarisation. For $\sigma = 0.75$ e/Ω, the distortions are very close to the bulk values. We can see from the plot that surface layers behave differently to the inner layers of the thin film. For each 2DEG calculation, the average distortion of the inner layers was used to calculate the effective polarisation. The layer-by-layer polarisation was also calculated (for more details, see Appendix A of [32]).

Figure 3.6 shows the layer-by-layer polarisation for a 2DEG of surface charge $\sigma = 0.75\ e/\Omega$.

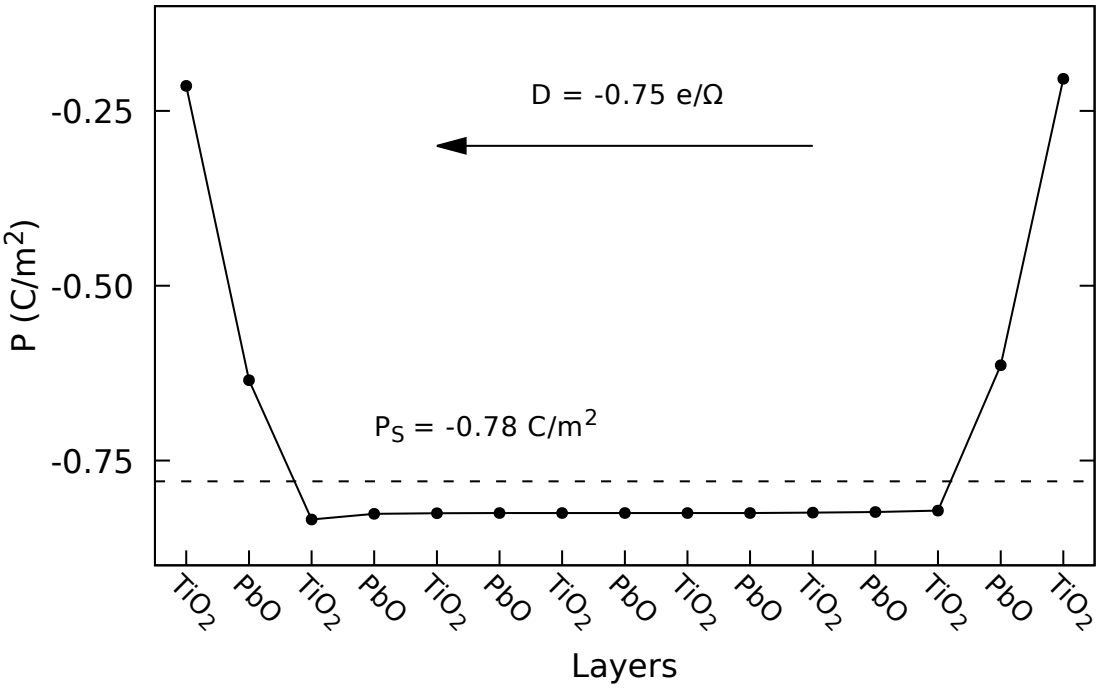

Fig. 3.6 The layer-by-layer polarisation of a thin film of PTO with a 2DEG of $\sigma = 0.75\ e/\Omega$, calculated using the methods described in [32]. The polarisation of the surface layers has been neglected.

Again to avoid surface effects, we average over the inner layers. The two previous plots show that, for surface charges close to the spontaneous polarisation, the distortion and polarisation approach those of the bulk configuration. The polarisations were calculated as a function of surface charge using both methods and are shown in Figure 3.7.

There are a few important features of this plot to note. Firstly, at zero surface charge there is a nonzero residual polarisation, which is in agreement with our analysis of the first plot in 3.4. The residual polarisation was not obtained using the layer-by-layer calculation, however. The polarisation increases linearly with the surface charge until $\sigma = P_S$, above which we would expect the polarisation to saturate. This saturation was expected to occur earlier, however it might be because the spontaneous polarisation that would have been obtained using the computational parameters in this study result in a larger value than the one from [14]. Just above P_S, the polarisation increases in a linear regime, beyond which it begins to saturate. From the small electric field in the lower plot of 3.4 and the polarisation close to P_S in 3.7, we can conclude that the introduction of a 2DEG using the VCA has had the expected effect

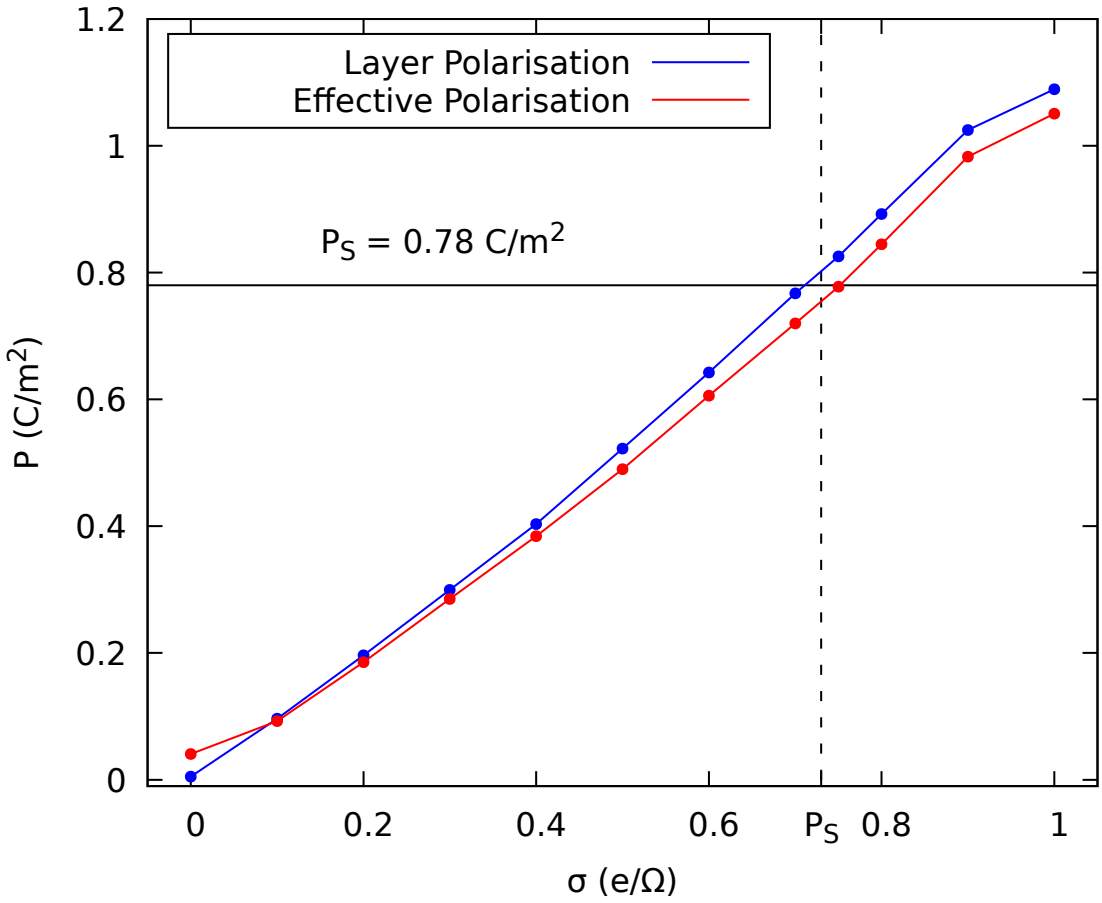

Fig. 3.7 Polarisation as a function of 2DEG surface charge for a thin film of PTO. Shown in blue is the layer-by-layer polarisation calculated using the Born effective charges of cubic bulk PTO. The effective polarisation associated with the distortion of the layers is shown in red; the polarisations of the PbO and TiO_2 layers were calculated separately and the average value was taken. The horizontal is at the spontaneous polarisation of bulk PTO from [14]. The dashed line indicates the value of σ that corresponds to this spontaneous polarisation.

of screening the depolarising field in the thin films and sustaining the polarisation.

Similar results were obtained for the superlattice calculations and are summarised in Figure 3.8. One noticeable difference between our expectations from the theory and the computational results is the electrostatic potential inside the superlattice. We expected the potential to have a zig-zag-type form. However, it appears that there is little or no electric field inside the superlattice. The only place where there is an electric field is at the interfaces between the layers, indicating that there is an interfacial transfer of charge. Surface and interfacial effects are of a quantum nature and were not accounted for in our macroscopic theory developed in the previous chapter.

Reference [16] performed a similar first-principles study of LAO/STO superlattices and observed a zig-zag-type potential. However, the origin of the 2DEG in LAO/STO is different. In LAO/STO, there is an intrinsic surface charge at the interfaces, whereas we manually introduced the 2DEG using the VCA. Our plot of the potential inside the film is a combination of both the polarisation and surface charges, which are of similar magnitude and opposite direction. In order to observe this type of potential inside the film, we would need to separate the two.

Nevertheless, we see that the superlattice is still insulating, and we also see the distortion and hence polarisation of the PTO layers, while the STO layers remain relatively unaffected, as expected.

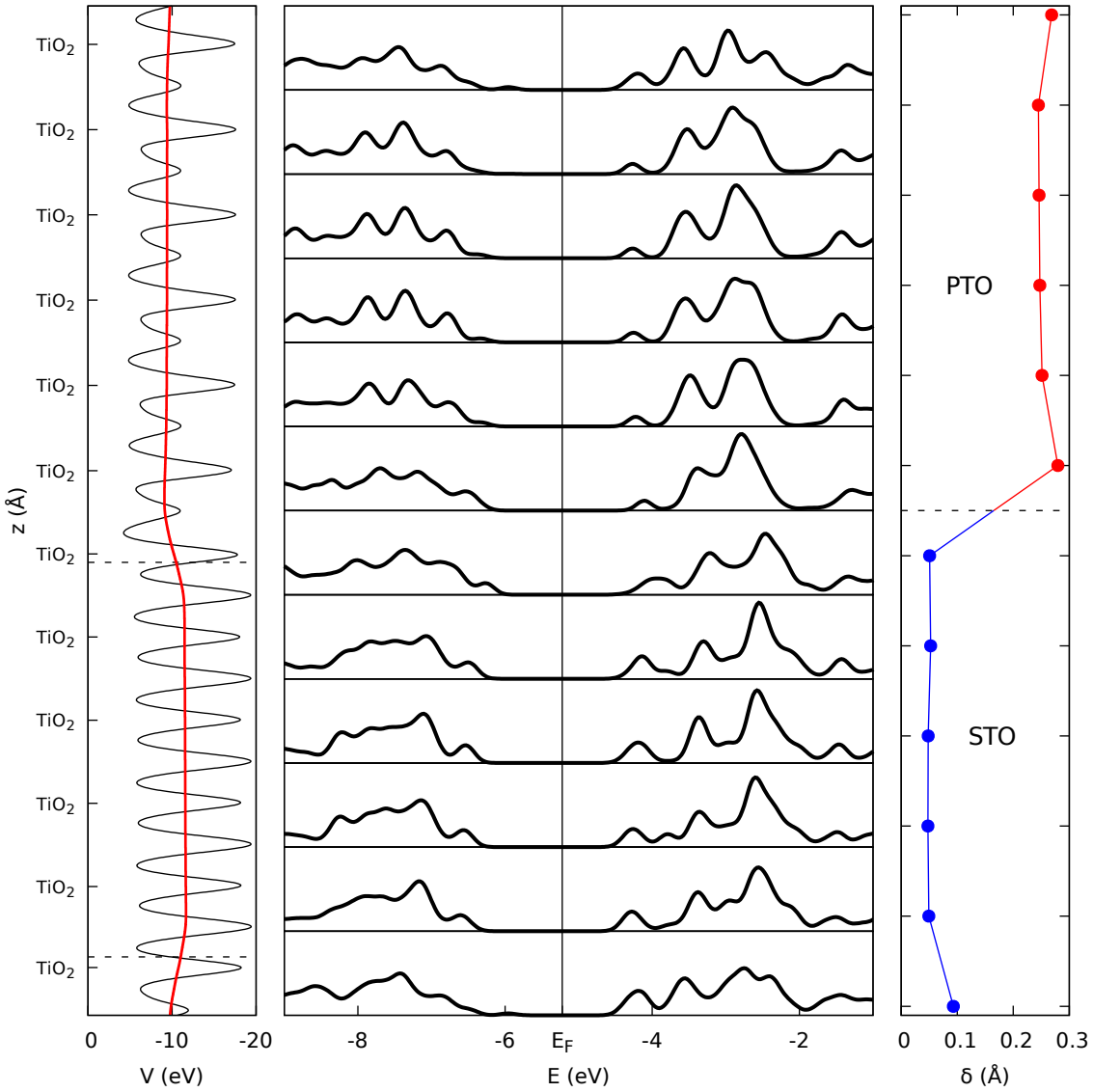

Fig. 3.8 A summary of results for a superlattice comprised of 6 layers of PTO and 6 layers of STO. Left: the planar averaged and nanosmoothed electrostatic potentials. The interfaces between the two materials are indicated with the dashed lines. Middle: the PDOS of the TiO_2 layers in the superlattice. We see that the Fermi level remains in the gap throughout the unit cell. Right: the distortion of the TiO_2 layers.

Chapter 4

Conclusions

We derived expressions for the electrostatic depolarising energy of a ferroelectric thin film on a substrate and a superlattice. These expressions exhibited the expected monodomain behaviour, and reproduced the expressions for a thin film in a vacuum in the appropriate limits. Having obtained these energies, Kittel approximations to the electrostatics were obtained in the polydomain limit. These approximations led to a modified Kittel law, which described the behaviour of the domains in thin films on substrates and in superlattices. This could prove very useful for analysing experimental results of domains in ferroelectric thin films and superlattices.

The Landau theory of coexistence between screening mechanisms was also modified to account for substrates and describe superlattices. It was found that the permittivities of the substrate and the paraelectric layers in the superlattice can extend the range of thicknesses where coexistence can be sustained. In the case of superlattices, further modifications to the model may be required to describe effects which are unique to superlattices and may not be observed in thin films. Examples of such effects are the induced domain structure in the paraelectric layers and a charge transfer at the interfaces between the layers.

First-principles calculations were performed for monodomain thin films of PTO in a vacuum and PTO/STO superlattices. Concentrations of surface defects were introduced to a single unit cell using the VCA, and we observed the screening of the depolarising field and sustaining of the polarisation by the 2DEGs. For the superlattice calculations, a charge transfer was observed at the interfaces even in the absence of a 2DEG, indicating that a more detailed study of interfacial effects is required.

4.1 Further Work

The results presented suggest that there is much to be done in terms of further work, the most obvious of which is to verify our theories against experiment. It would be very useful to see if our modified Kittel laws can describe the behaviour of domains in thin films and superlattices more accurately than the standard Kittel law for a thin film in a vacuum. It is also important that we observe the coexistence of screening mechanisms experimentally, validating our model. Experiments on PTO/STO superlattices may give an insight into effects unique to superlattices that we did not consider when extending the Landau theory from the thin film.

In terms of theory, there are many possibilities for extending the model. For example, when studying coexistence between domains and the 2DEG, we fixed the polarisation at the spontaneous polarisation, ensuring the materials were in a stable ferroelectric state. Allowing the polarisation to vary may give us a more complete picture of coexistence, although this would result in a Landau theory which is not analytically solvable, meaning we would have to rely on numerical solutions. Since we started with the coexistence model for a thin film in a vacuum and extended it to describe thin films on substrates and superlattices, there are a number of effects unique to those systems which we may not have accounted for. The most obvious one is the misfit strain caused by the difference in lattice constant between the thin film and the substrate or the layers in the superlattice. This should be accounted for by including the energy associated with the misfit strain in the Landau theory, and by studying the strain associated with forming commensurate structures through first-principles calculations.

For the superlattice calculations, a full unit cell relaxation was performed, and we assumed that the PTO and STO layers formed a commensurate structure. However, these effects could be very important, as there is a strong coupling between strain and polarisation in ferroelectric materials. For the superlattices, there may be an induced domain structure in the paraelectric layers. We expect the energy associated with this domain structure to be much weaker than the one for the ferroelectric layers, but it could still have an impact on the coexistence of the screening mechanisms, so it should be included in the Landau theory. The first-principles calculations of superlattices showed a charge transfer across the interfaces between the layers. The nature of this effect and its relation to the 2DEG should be studied in greater detail; it may be that there is a higher-order dependence on the 2DEG which has not been accounted for.

The work presented here has laid the groundwork for a more detailed computational study of screening mechanisms in ferroelectric materials. As we have extended our theoretical model to describe thin films on substrates, it would be useful to do the same thing computationally, and compare our calculations for PTO in a vacuum to PTO on a substrate of STO. As mentioned above, it is necessary to study the effects of misfit strain in order to extend our theory of coexistence. A more detailed first-principles study of PTO/STO superlattices might prove insightful with regard to the induced domain structure in the STO layers and the charge transfer at the interfaces. In order to study coexistence computationally, it is necessary to introduce ferroelectric domains to our calculations. It would also be preferable to replace the surface charge introduced with the VCA, with oxygen and cation vacancies at the interfaces. While we have verified that our systems are still insulating, introducing the surface charges through real defects would result in more realistic simulations. Both domains and defects require large supercell calculations, increasing the computational resources and time required substantially, especially when performing geometry relaxations. However, the geometries obtained can be used in the supercell calculations and could greatly reduce the number of geometry relaxation steps required. It might prove useful to study the behaviour of the domains using other computational methods, such as (ab-initio) molecular dynamics and phase-field modelling.

In summary, screening mechanisms observed in ferroelectric materials have been studied and observed through both theory and computational simulations. We have presented a more realistic treatment of the electrostatics of ferroelectric materials which takes into account the substrates on which thin films are grown, and the geometry of the superlattices in which they are often fabricated. The competition and coexistence of these screening mechanisms were then studied using a more realistic model, and first-principles calculations were performed to observe the effects of a 2DEG on monodomain thin films of PTO and PTO/STO superlattices.

References

[1] N. Setter, D. Damjanovic, L. Eng, G. Fox, S. Gevorgian, S. Hong, A. Kingon, H. Kohlstedt, N. Park, G. Stephenson, *et al.*, "Ferroelectric Thin Films: Review of Materials, Properties, and Applications," *Journal of Applied Physics*, vol. 100, no. 5, p. 051606, 2006.

[2] J. F. Scott and C. A. P. De Araujo, "Ferroelectric Memories," *Science*, vol. 246, no. 4936, pp. 1400–1405, 1989.

[3] P. Muralt, "Ferroelectric Thin Films for Micro-Sensors and Actuators: A Review," *Journal of Micromechanics and Microengineering*, vol. 10, no. 2, p. 136, 2000.

[4] D. Dausch and G. Haertling, "Bulk vs. Thin Film PLZT Ferroelectrics," in *Applications of Ferroelectrics, 1992. ISAF'92., Proceedings of the Eighth IEEE International Symposium on*, pp. 297–300, IEEE, 1992.

[5] J. Kwo, E. Gyorgy, D. McWhan, M. Hong, F. DiSalvo, C. Vettier, and J. Bower, "Magnetic and Structural Properties of Single-Crystal Rare-Earth Gd-Y Superlattices," *Physical Review Letters*, vol. 55, no. 13, p. 1402, 1985.

[6] K. Iijima, T. Terashima, Y. Bando, K. Kamigaki, and H. Terauchi, "Atomic Layer Growth of Oxide Thin Films with Perovskite-Type Structure by Reactive Evaporation," *Journal of Applied Physics*, vol. 72, no. 7, pp. 2840–2845, 1992.

[7] T. Tsurumi, T. Suzuki, M. Yamane, and M. Daimon, "Fabrication of Barium Titanate / Strontium Titanate Artificial Superlattice by Atomic Layer Epitaxy," *Japanese Journal of Applied Physics*, vol. 33, no. 9S, p. 5192, 1994.

[8] A. Tagantsev, I. Stolichnov, E. Colla, and N. Setter, "Polarization Fatigue in Ferroelectric Films: Basic Experimental Findings, Phenomenological Scenarios, and Microscopic Features," *Journal of Applied Physics*, vol. 90, no. 3, pp. 1387–1402, 2001.

[9] J. Junquera and P. Ghosez, "Critical Thickness for Ferroelectricity in Perovskite Ultrathin Films," *Nature*, vol. 422, no. 6931, p. 506, 2003.

[10] A. Ohtomo, D. Muller, J. Grazul, and H. Y. Hwang, "Artificial Charge-Modulation in Atomic-Scale Perovskite Titanate Superlattices," *Nature*, vol. 419, no. 6905, p. 378, 2002.

[11] A. Ohtomo and H. Hwang, "A High-Mobility Electron Gas at the $LaAlO_3/SrTiO_3$ Heterointerface," *Nature*, vol. 427, no. 6973, p. 423, 2004.

[12] N.-G. Park, "Perovskite Solar Cells: an Emerging Photovoltaic Technology," *Materials Today*, vol. 18, no. 2, pp. 65–72, 2015.

[13] A. K. Tagantsev, L. E. Cross, and J. Fousek, *Domains in Ferroic Crystals and Thin Films*. Springer, 2010.

[14] P. Aguado-Puente, N. Bristowe, B. Yin, R. Shirasawa, P. Ghosez, P. B. Littlewood, and E. Artacho, "Model of Two-Dimensional Electron Gas Formation at Ferroelectric Interfaces," *Physical Review B*, vol. 92, no. 3, p. 035438, 2015.

[15] B. Yin, P. Aguado-Puente, S. Qu, and E. Artacho, "Two-Dimensional Electron Gas at the $PbTiO_3/SrTiO_3$ Interface: An Ab Initio Study," *Physical Review B*, vol. 92, no. 11, p. 115406, 2015.

[16] N. Bristowe, E. Artacho, and P. Littlewood, "Oxide Superlattices with Alternating p and n Interfaces," *Physical Review B*, vol. 80, no. 4, p. 045425, 2009.

[17] C. Kittel, "Theory of the Structure of Ferromagnetic Domains in Films and Small Particles," *Physical Review*, vol. 70, no. 11-12, p. 965, 1946.

[18] M. Muñoz Basagoiti, P. Aguado-Puente, and E. Artacho, "Coexistence of the Two-Dimensional Electron Gas and Ferroelectric Domains in Ferroelectric Thin Films." Masters Dissertation, 2017.

[19] D. Fuchs, C. Schneider, R. Schneider, and H. Rietschel, "High Dielectric Constant and Tunability of Epitaxial $SrTiO_3$ Thin Film Capacitors," *Journal of Applied Physics*, vol. 85, no. 10, pp. 7362–7369, 1999.

[20] R. O. Jones, "Density Functional Theory: Its Origins, Rise to Prominence, and Future," *Reviews of Modern Physics*, vol. 87, no. 3, p. 897, 2015.

[21] L. Bellaiche and D. Vanderbilt, "Virtual Crystal Approximation Revisited: Application to Dielectric and Piezoelectric Properties of Perovskites," *Physical Review B*, vol. 61, no. 12, p. 7877, 2000.

[22] S. De Gironcoli, P. Giannozzi, and S. Baroni, "Structure and Thermodynamics of Si_xGe_{1-x} Alloys from Ab Initio Monte Carlo Simulations," *Physical Review Letters*, vol. 66, no. 16, p. 2116, 1991.

[23] E. I. Isaev, S. I. Simak, I. Abrikosov, R. Ahuja, Y. K. Vekilov, M. Katsnelson, A. Lichtenstein, and B. Johansson, "Phonon Related Properties of Transition Metals, their Carbides, and Nitrides: A First-Principles Study," *Journal of Applied Physics*, vol. 101, no. 12, p. 123519, 2007.

[24] L. Bellaiche, S.-H. Wei, and A. Zunger, "Band Gaps of GaPN and GaAsN Alloys," *Applied Physics Letters*, vol. 70, no. 26, pp. 3558–3560, 1997.

[25] N. J. Ramer and A. M. Rappe, "Application of a New Virtual Crystal Approach for the Study of Disordered Perovskites," *Journal of Physics and Chemistry of Solids*, vol. 61, no. 2, pp. 315–320, 2000.

[26] B. Meyer and D. Vanderbilt, "Ab Initio Study of $BaTiO_3$ and $PbTiO_3$ Surfaces in External Electric Fields," *Physical Review B*, vol. 63, no. 20, p. 205426, 2001.

[27] J. M. Soler, E. Artacho, J. D. Gale, A. García, J. Junquera, P. Ordejón, and D. Sánchez-Portal, "The SIESTA Method for Ab Initio Order-N Materials Simulation," *Journal of Physics: Condensed Matter*, vol. 14, no. 11, p. 2745, 2002.

[28] D. M. Ceperley and B. Alder, "Ground State of the Electron Gas by a Stochastic Method," *Physical Review Letters*, vol. 45, no. 7, p. 566, 1980.

[29] N. Troullier and J. L. Martins, "Efficient Pseudopotentials for Plane-Wave Calculations," *Physical Review B*, vol. 43, no. 3, p. 1993, 1991.

[30] H. J. Monkhorst and J. D. Pack, "Special Points for Brillouin-Zone Integrations," *Physical Review B*, vol. 13, no. 12, p. 5188, 1976.

[31] A. Garcıa, "ATOM User Manual," 2008.

[32] M. Stengel, P. Aguado-Puente, N. A. Spaldin, and J. Junquera, "Band Alignment at Metal/Ferroelectric Interfaces: Insights and Artifacts from First Principles," *Physical Review B*, vol. 83, no. 23, p. 235112, 2011.

[33] A. Baldereschi, S. Baroni, and R. Resta *Physical Review Letters*, vol. 61, no. 6, p. 734, 1988.

[34] L. Colombo, R. Resta, and S. Baroni, "Valence-Band Offsets at Strained Si/Ge Interfaces," *Physical Review B*, vol. 44, no. 11, p. 5572, 1991.

[35] Z. Wu, R. Cohen, and D. Singh, "Comparing the Weighted Density Approximation with the LDA and GGA for Ground-State Properties of Ferroelectric Perovskites," *Physical Review B*, vol. 70, no. 10, p. 104112, 2004.

[36] J. Rodriguez, A. Etxeberria, L. González, and A. Maiti, "Structural and Electronic Properties of $PbTiO_3$, $PbZrO_3$, and $PbZr_{0.5}Ti_{0.5}O_3$: First-Principles Density-Functional Studies," *The Journal of Chemical Physics*, vol. 117, no. 6, pp. 2699–2709, 2002.

[37] S. Tinte, K. M. Rabe, and D. Vanderbilt, "Anomalous Enhancement of Tetragonality in $PbTiO_3$ Induced by Negative Pressure," *Physical Review B*, vol. 68, no. 14, p. 144105, 2003.

[38] B. Meyer and D. Vanderbilt, "Ab Initio Study of Ferroelectric Domain Walls in $PbTiO_3$," *Physical Review B*, vol. 65, no. 10, p. 104111, 2002.

[39] F. Jona and G. Shirane, *Ferroelectric Crystals*, vol. 1. Pergamon, 1962.

Appendix A

Computational Details and Bulk PTO

This appendix contains additional information about the computational details of the first-principles calculations and the results of the bulk PTO calculations. All calculations were performed using SIESTA version 4.1-b3 on the CSD3 cluster. Calculations were performed in parallel with OpenMP across a single node (32 cores). Details about the compilation of SIESTA and the machines on which the calculations were performed are included in the supplementary material.

Table A.1 details the valence configurations and cutoff radii of the pseudopotentials used in the DFT calculations. Scalar relativistic pseudpotentials were generated for the Pb, Sr and Ti atoms, and a non-relativistic pseudopotential was generated for the O atoms. The same reference configuration and cutoff radii were used when generating the mixed pseudopotentials with the VCA.

Table A.1 Reference configurations and cutoff radii (in bohr) for the pseudopotentials used in this work. The configuration and cutoff radii for oxygen were used for the virtual atoms generated using the VCA.

		Pb	Sr	Ti	O
Reference		$6s^2, 6p^2, 5d^{10}, 5f^0$	$4s^2, 4p^6, 4d^0, 4f^0$	$3s^2, 3p^6, 3d^2, 4f^0$	$2s^2, 2p^4, 3d^0, 4f^0$
Radius	s	2.2	1.5	1.3	1.15
	p	2.9	1.5	1.3	1.15
	d	1.5	2.0	1.3	1.15
	f	2.9	2.0	2.0	1.50

Basis sets for the atoms included single-zeta basis functions for the semicore electrons and double-zeta polarised basis functions for the basis electrons. The basis for oxygen was also used for the virtual atoms. Full details of the basis sets can be found in the input files included in the supplementary material.

The ferroelectric structure of bulk PTO was obtained using geometry relaxations. The results are compared to similar calculations in the literature in Table A.2. The in-plane lattice constant is in good agreement with other first-principles in the literature, but underestimates the experimental value. This is not surprising, as LDA calculations typically underestimate unit cell volumes. The ratio c/a gives a strain of 5%, which is close to the expected value of 6%. There is a large variance in the distortions of the layers. However, this is expected as the results of similar DFT calculations depend strongly on the exchange-correlation functional and other computational parameters used. The effective polarisations of the thin films were calculated using the bulk values of the distortions and were in agreement with the layer-by-layer polarisations calculated using the Born effective charges. Because of this, we can conclude that our values are reliable, or are at least consistent within the framework of our first-principles calculations.

Table A.2 A comparison of results for the structure of ferroelectric bulk PTO between this work and the literature and experiment.

Reference	a (Å)	c (Å)	δ_z(PbO) (Å)	δ_z(TiO_2) (Å)
Wu [35]	3.87	4.03	0.332	0.275
Rodriguez [36]	3.86	4.13	0.410	0.335
Tinte [37]	3.86	4.00	0.302	0.239
Vanderbilt [38]	3.86	4.04	0.372	0.277
This Work	3.86	4.07	0.356	0.297
Experiment [39]	3.90	4.15	0.460	0.292